# On the design of non-Hermitian elastic metamaterial for broadband perfect absorbers

Liyun Cao, Yifan Zhu, Sheng Wan, Yi Zeng, Badreddine Assouar

## To cite this version:

Liyun Cao, Yifan Zhu, Sheng Wan, Yi Zeng, Badreddine Assouar. On the design of non-Hermitian elastic metamaterial for broadband perfect absorbers. International Journal of Engineering Science, 2022, 181, pp.103768. 10.1016/j.ijengsci.2022.103768 . hal-03843361

HAL Id: hal-03843361

https://hal.science/hal-03843361

Submitted on 8 Nov 2022

# On the Design of Non-Hermitian Elastic Metamaterial for Broadband Perfect Absorbers

Liyun Cao *, Yifan Zhu, Sheng Wan, Yi Zeng, Badreddine Assouar*

**Keywords**: elastic metamaterials, non-Hermitian, broadband, low-frequency, perfect absorption

## Abstract

Elastic metamaterial, an engineered artificial material, has received much attention in physics and engineering communities due to its functional properties unavailable in natural materials. However, most elastic metamaterials, especially for their two-dimensional structures, belong to the Hermitian category, making them difficult to adapt to real lossy structures and explore their loss modulation. In the present study, non-Hermitian loss-modulation beam and plate models based on complex wavenumber plane, structural dynamics, and mode-coupling scattering theory are established to design lossy elastic metamaterials (LEMs) for any solid material. Based on a unified closed-form solution for absorption, the subwavelength loss-modulation LEM can cope with the conventional challenge of achieving broadband and near-omnidirectional elastic wave perfect absorption. We reveal here the high-performance absorption of the LEM from greatly enhanced wave-energy dissipation by a combination of dissipation-radiation-balance and multiple reflections in the non-Hermitian elastic wave system. We numerically and experimentally verify the effectiveness of the theoretical model and demonstrate broadband and perfect absorption in a plate-like structure. Our work not only opens a new route to achieve broadband low-frequency vibration suppression in macro devices and microelectromechanical systems, more essentially, but it also provides an effective paradigm to wave engineering in non-Hermitian elastic wave systems.

## 1. Introduction

Ongoing development of elastic metamaterials (Assouar et al., 2018; Chen et al., 2021; Dong et al., 2022; Zhu et al., 2014) and metasurfaces (Cao et al., 2020; Lee et al., 2018; Liu et al., 2017; Rong et al., 2020) has opened up new possibilities to control elastic waves scattering (solid object dynamic deform), which provides functional properties unavailable in natural materials. However, in most elastic metamaterial (Dong et al., 2021; Muhammad et al., 2020; Zeng et al., 2021; Zhao et al., 2021) or metasurface (Cao et al., 2021d; Jin et al., 2021; Li et al., 2020a; Liu et al., 2021; Ruan and Liang, 2021; Shen et al., 2021; Yuan et al., 2020; Zhang et al., 2020), especially for their two-dimensional structures, the modulation of inherent loss is ignored because of the tiny damping of pure metal media. The corresponding systems are consequently treated as Hermitian, which are widely used to describe a closed physical system with respect to energy conservation. In a practical system, most solid structures are metal alloys and composites or introduce additional damping layers, which naturally have inevitable dissipation. Lately, considering loss modulation, the non-Hermitian description (Gu et al., 2021; Hu et al., 2021b; Liu et al., 2019; Wang et al., 2021a) has attracted growing attention in exploring new physics in the non-conservation system of optical waves

(Kawabata et al., 2019; Wang et al., 2021a) and acoustic waves (Merkel et al., 2015; Romero-García et al., 2016; Zhou et al., 2021), for example, unidirectional invisibility (Li et al., 2020b; Lin et al., 2011), enhanced sensing (Chen et al., 2017; Nair et al., 2021), topological characteristics (Hu et al., 2021a; Wang et al., 2021b) and asymmetric transmission (Li et al., 2017).

Mechanical vibration absorption of beam/plate-type structures is a conventional research topic. It has been widely investigated since the early 1950s, because of considerable significance in many engineering applications, for example, preventing vibration-induced fatigue damage, eliminating vibration interference to high-precision instruments, and fundamentally reducing noise sources. However, with the development of elastic-wave-based information technology in microelectromechanical devices and chip sensors in recent years, it is difficult for the conventional vibration absorption methods to meet the needs of lightweight and miniaturization. The conventional vibration absorption methods are represented by attaching many damping layers (Kerwin, 1959; Sun et al., 1995) and heavy dynamic vibration absorbers (Hunt and Nissen, 1982; Shen et al., 2019). As a newly generated method of vibration absorption, the acoustic black hole (Deng and Zheng, 2022; Gao et al., 2021; McCormick and Shepherd, 2019; Pelat et al., 2020; Tang et al., 2016) is not useful for the low-frequency range (long wavelength) because its large structure dimension seriously hampers practical applications. Afterward, a sub-wavelength resonator (Leng et al., 2019) with an attached damping layer in one-dimensional elastic beams was proposed to achieve perfect absorption of flexural waves in one specific frequency. A broadband active meta-layer (Li et al., 2021b) composed of piezoelectric sensors and actuators with complex feedback control loops in an elastic beam was also proposed for flexural wave absorption in a high-frequency range. However, narrowband or no ability to apply low frequencies is their weakness. To date, it is still a great challenge to realize subwavelength lightweight structures for broadband vibration absorption in the low-frequency regime. The loss modulation in non-Hermitian systems is a possible way to break through the challenge.

In the present research, we establish a unified non-Hermitian model for engineered elastic beam/plate-type structures and design subwavelength lightweight lossy elastic metamaterial (LEM) to break through the challenge of broadband vibration absorption in low frequency. Based on the theoretical model, we discuss the loss-modulation-induced perfect absorption physics and analytically derive the perfect absorption condition. Combined with weak coupling between multi-resonators, the absorption bandwidth of LEM is enlarged in a beam-type structure. Further, we achieve broadband and near-omnidirectional perfect absorption in a plate-type structure by the LEM with the coaction of dissipation-radiation-balance FP resonance and multiple reflections of the $0^{\text{th}}$ diffraction mode. Based on the theoretical model, we also show asymmetrical perfect absorption at the exceptional point. The theoretical models are validated by the corresponding experimental and simulation results.

## 2. The model of the non-Hermitian elastic wave system

Fig. 1(a) illustrates a typical lightweight absorber composed of a waveguide resonator with the length $L$ on the edge of the background elastic beam. The background elastic beam with thickness $d$ and width $b$ occupies the volume $-\infty < x < 0$, $|y| \leq b/2$ and $|z| \leq d/2$ in the Cartesian coordinate system $\mathbf{x} = (x, y, z)$. Within the classical Bernoulli–Euler beam assumptions, the elastic wave (flexural wave) is specified by the displacement vector $\mathbf{u} = (0, 0, w)$, where $w(x, t)$ is a 1D (one-dimensional) function on the central axis $-\infty < x < L$, $y$=0, $z$=0. The function $w(x, t)$ obeys the governing equations:

$$\left( \frac{\partial}{\partial x^4} + \beta^4 \right) w(x,t) = 0 \tag{1}$$

where $\beta$ is the propagation constant, $\beta^4 = \rho d / D$. $D$ is the bending rigidity. $k = \beta\sqrt{\omega}$ is flexural wavenumber and $\omega$ is the angular frequency. Along with the Bernoulli–Euler beam, Eq. (1) with $\beta^4 = \rho d \big/ \left[ D\left(1-\upsilon^2\right) \right]$ is valid for a Kirchhoff plate of thickness $d$ [25]. The $\beta$ in Eq. (1) differs only by the factor $\left(1-\upsilon^2\right)$ in the elastic beam and plate, where $\upsilon$ is Poisson's ratio. Therefore, theoretical models of the elastic beam are also applicable to the elastic plate for the vertically incident wave. We should point out that the fourth-order partial derivative equation Eq. (1), unlike the two-order one in optics/acoustics, has four solutions of wavenumber, i.e., two real ones and two extra pure imaginary ones. The imaginary ones are intrinsic non-propagation modes, i.e., flexural evanescent waves (Graff, 1975), which hybridize scattering fields at all boundaries and interfaces of the elastic beam (plate) model. This makes the theoretical elastic wave model more complex and challenging than optic and acoustic ones.

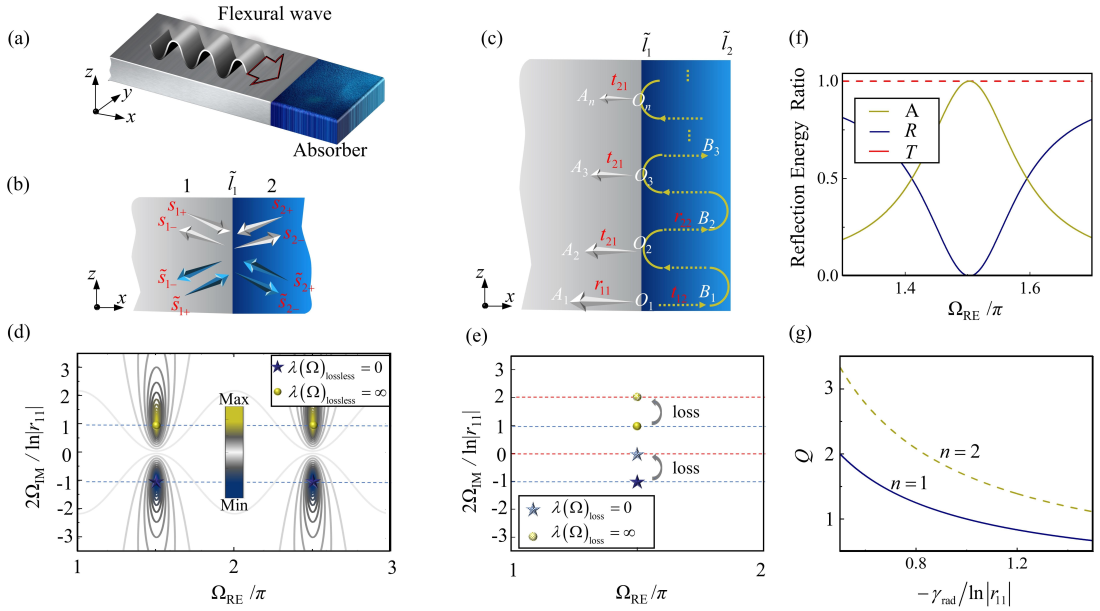

**Fig. 1.** Theoretical model. (a) A background elastic beam model (thickness $d_1$ and width $b$) with a waveguide resonator (length $L$ and thickness $d_2$) absorbing flexural wave. (b) The interface $\tilde{l}_1$ between the background beam (region 1) and waveguide resonator (region 2) scatters incoming propagation waves with amplitudes $s_{1+}$, $s_{2+}$, incoming evanescent ones with amplitudes $\tilde{s}_{1+}$, $\tilde{s}_{2+}$, outgoing propagation ones with amplitudes $s_{1-}$, $s_{2-}$, and outgoing evanescent ones with amplitudes $\tilde{s}_{1-}$, $\tilde{s}_{2-}$, respectively. (c) Reflection of flexural waves in the waveguide resonator. (d) and (e) The contour plots illustrating the distribution of $\ln\lambda_s$ in the lossless and lossy scattering system, respectively [Here, $\kappa = 0.6$, Đ$= 0.1$]. (f) The reflection energy ratio $|R|^2$ and absorption spectrum $\alpha$. (g) $Q$ varying with $\gamma_{\mathrm{rad}}$.

First, for an elastic wave system without loss, according to the continuities of displacement, slope, bending moment, shear force at the interface $\tilde{l}_1$ between the background beam and the waveguide resonator, we get the scattering equation of the interface

$$\mathbf{S}^- = \begin{pmatrix} t_{12} & r_{22} & t_{\tilde{1}2} & r_{\tilde{2}2} \\ r_{11} & t_{21} & r_{\tilde{1}1} & t_{\tilde{2}1} \\ t_{1\tilde{2}} & r_{2\tilde{2}} & t_{\tilde{1}\tilde{2}} & r_{\tilde{2}\tilde{2}} \\ r_{1\tilde{1}} & t_{2\tilde{1}} & r_{\tilde{1}\tilde{1}} & t_{\tilde{2}\tilde{1}} \end{pmatrix} \mathbf{S}^+ = \mathbf{M}_{\mathrm{I}} \cdot \mathbf{S}^+, \tag{2}$$

where $\mathbf{S}^- = [s_{2-}, s_{1-}, \tilde{s}_{2-}, \tilde{s}_{1-}]^T$ and $\mathbf{S}^+ = [s_{1+}, s_{2+}, \tilde{s}_{1+}, \tilde{s}_{2+}]^T$. $\mathbf{M}_{\mathrm{I}}$ is the scattering matrix. The symbols $t$ and $r$ denote the transmission and reflection coefficients, respectively. The subscripts 1 and 2 represent the background beam and the absorber, as shown in

Fig. 1(b). The superscript ~ represents the evanescent mode. The scattering coefficients are functions of wavenumber ratio $\kappa = k_1/k_2$ and flexural stiffness ratio $Đ = D_1/D_2$, which are determined by the material parameters $E_{1(2)}$, $\rho_{1(2)}$, $\upsilon_{1(2)}$, and geometric parameters $d_{1(2)}$ of the model. $k_{1(2)} = \beta_{1(2)}\sqrt{\omega}$ is flexural wavenumber and $\omega$ is the angular frequency. Analytical expressions of all scattering coefficients in $\mathbf{M}_\mathrm{I}$ can be found in Appendix A.

In the one-port elastic wave system, the incident wave is divided into two sub-waves at the interface $\tilde{l}_1$ in Fig. 1(c), one reflected in the direction $O_1A_1$ and the other transmitted into the resonator in the direction $O_1B_1$. The latter is reflected on the right boundary $\tilde{l}_2$ and is then divided into two sub-waves at the interface $\tilde{l}_1$ again, one transmitted in the direction $O_2A_2$, the other reflected into the resonator in the direction $O_2B_2$; and the process of the wave division remaining inside the resonator continues, as indicated in Fig. 1(c). The total reflection field is formed by multiple reflections from the interfaces $\tilde{l}_1$ and $\tilde{l}_2$. Based on Eq. (2), the reflection coefficient $R$ equals the sum of reflection coefficients of $\bar{N}$ $(\bar{N} \to \infty)$ sub-waves from the interfaces $\tilde{l}_1$ [65]

$$R = r_{11} + \sum_{\bar{N}=1}^{\infty} t_{12}t_{21}e^{-i\phi} \cdot \left(r_{22}e^{-i\phi}\right)^{\bar{N}-1} = r_{11} + \frac{t_{12}t_{21}e^{-i\phi}}{1 - r_{22}e^{-i\phi}}, \tag{3}$$

where $\phi = 2k_2L - 3\pi/2$ is the phase of the wave propagating a round-trip between the interfaces $\tilde{l}_1$ and $\tilde{l}_2$. We should point out that Eq. (3) does not consider the near-field evanescent wave interference due to $L$ being more than the half wavelength. Yet, it includes the contribution of the evanescent wave hybridization in all boundaries and interfaces. For example, $3\pi/2$ in the above expression of $\phi$ is the phase shift of the flexural wave at the boundary $\tilde{l}_2$, which is from the evanescent wave hybridization (see detailed derivation in Appendix G). However, optic/acoustic waves at a similar boundary have no phase shift.

The eigenvalue of the one-port elastic wave system equals the magnitude of the complex reflection coefficient, i.e., $\lambda_s = |R|$. After substituting a dimensionless complex wavenumber $\Omega = k_2 L = \left(\tilde{k}_{\mathrm{RE}} + \tilde{k}_{\mathrm{IM}}\mathrm{i}\right)L$ into Eq. (3), $\lambda_s = |R|$ becomes a function of both real wavenumber $\Omega_{\mathrm{RE}}$ and imaginary wavenumber $\Omega_{\mathrm{IM}}$. A contour plot illustrating the distribution of $\ln\lambda_s$ is shown in Fig. 1(d). In the complex wavenumber plane, Zero corresponds to the eigenvalue $|\lambda_s(\Omega)| = 0$. $\lambda_s$ satisfies $\lambda_s^*(\Omega) = 1/\lambda_s(\Omega^*)$, in which * represents the conjugate. Pole corresponds to the eigenvalue $|\lambda_s(\Omega^*)| = \infty$. Therefore, a pair of Zero and Pole are symmetrically distributed about the real wavenumber axis, as shown in Fig. 1(d). The corresponding wavenumbers of Pole and Zero can be expressed as (see detailed derivation in Appendix B)

$$\Omega_{\mathrm{Pole}}^{\mathrm{Lossless}} = \varphi - \frac{\ln|r_{11}|}{2}\cdot\mathrm{i}, \tag{4}$$

$$\Omega_{\mathrm{Zero}}^{\mathrm{Lossless}} = \varphi + \frac{\ln|r_{11}|}{2}\cdot\mathrm{i}, \tag{5}$$

where

$$\varphi = \frac{3\pi}{4} - \frac{1}{2}\arg\left(r_{11}\right) + n\pi,\ n \geq 1. \tag{6}$$

$n$=1 represents the first pair of Zero and Pole in the complex wavenumber plane. The $n^{\mathrm{th}}$ pair will shift $(n-1)\pi$ along the real wavenumber axis.

The imaginary part of the Pole represents the radiative decay constant $\Gamma_{\text{rad}} = \text{Im}\left(\Omega_{\text{Pole}}^{\text{Lossless}}\right)$ from the resonator to the background structure. The corresponding frequency of the Pole can be expressed as $\omega_{\text{Pole}}^{\text{Lossless}} = \left(\Omega_{\text{Pole}}^{\text{Lossless}}\right)^2 \sqrt{\frac{\text{Re}\left(D_2\right)}{\rho_2 h_2 L^4}}$. It indicates that the radiative wave in the resonator will decay in the function of $e^{\text{Im}\left(\omega_{\text{Pole}}^{\text{Lossless}}\right)\cdot t}$ at the frequency of $\text{Re}\left(\omega_{\text{Pole}}^{\text{Lossless}}\right)$. Therefore, the quality factor of the resonance due to radiation can be expressed as

$$Q_{\text{rad}} = \frac{1}{2}\text{Re}\left(\omega_{\text{Pole}}^{\text{Lossless}}\right)\tau_{\text{rad}} = \frac{\text{Re}\left(\omega_{\text{Pole}}^{\text{Lossless}}\right)}{2\cdot\text{Im}\left(\omega_{\text{Pole}}^{\text{Lossless}}\right)} = \frac{\text{Re}\left[\left(\Omega_{\text{Pole}}^{\text{Lossless}}\right)^2\right]}{2\cdot\text{Im}\left[\left(\Omega_{\text{Pole}}^{\text{Lossless}}\right)^2\right]}, \tag{7}$$

where $\tau_{\text{rad}}$ is finite lifetime, $\tau_{\text{rad}} = 1/\gamma_{\text{rad}} = 1/\text{Im}\left(\omega_{\text{Pole}}^{\text{Lossless}}\right)$. $\gamma_{\text{rad}}$ is radiative decay rate, which determines the resonance linewidth at its half-maximum (Sauvan et al., 2013). We should point out that for the resonator described by the first pair of Zero and Pole in Fig. 1(d), its $Q_{\text{rad}}$ is about 8.4 according to Eq. (7). Its reflection coefficient $|R|$ is a fixed value of one for all real wavenumbers due to the lossless. However, its reflection phase spectrum has a rapid change at the resonance frequency, which is consistent with the positive and negative of $\Omega_{\text{IM}}$ rapidly changes on the real axis $\Omega_{\text{RE}} = 3\pi/2$ of the complex wavenumber plane.

In the lossy non-Hermitian elastic wave system, for the resonator with the dissipative decay constant $\varsigma$, the complex reflection coefficient $R$ in Eq. (3) can be replaced as

$$R = r_{11} + \frac{t_{12}t_{21}e^{-i\phi'}}{1 - r_{22}e^{-i\phi'}}, \tag{8}$$

where $\phi'$ is the phase constant with loss modulation $\phi' = \phi - \varsigma \cdot \mathrm{i}$. When the dissipative decay constant satisfies $\varsigma = \Gamma_{\mathrm{rad}}$, the distribution of $\mathrm{In}\lambda_s$ in Fig. 1(d) will move up $\varsigma$. It is the dissipation-radiation-balance, like the so-called critical coupling (Cai et al., 2000) in the optic system, however, here it is fulfilled in a different physical system with evanescent mode hybridization. Zero is located on the real wavenumber axis, as shown in Fig. 1(e). It indicates that $\Omega$ is a real number, $\lambda_s = |R|$ can equal zero, i.e., existing a perfect absorption. The corresponding wavenumbers of Pole and Zero with loss modulation $\varsigma$ can be expressed as

$$\Omega_{\mathrm{Pole}}^{\mathrm{Loss}} = \varphi - \frac{\ln|r_{11}|}{2} \cdot \mathrm{i} + \varsigma \cdot \mathrm{i} = \varphi - \ln|r_{11}| \cdot \mathrm{i}, \tag{9}$$

$$\Omega_{\mathrm{Zero}}^{\mathrm{Loss}} = \varphi. \tag{10}$$

According to loss modulation $\varsigma$ of Eq. (10), the perfect absorption condition (PAC) in the non-Hermitian elastic wave system can be expressed as (see detailed derivation in Appendix C)

$$\frac{\mathrm{Re}(\wp)}{\mathrm{Im}(\wp)} \equiv \frac{2\varphi}{\ln|r_{11}|}, \tag{11}$$

where $\wp$ is the loss constant $\wp = \sqrt[4]{1 - \eta \cdot \mathrm{i}}$, and $\eta$ is the loss factor. Once the material parameters $E_{1(2)}$, $\rho_{1(2)}$, $\upsilon_{1(2)}$, geometric parameters $d_{1(2)}$, and loss factor $\eta$ meet PAC, the energy of the incident flexural wave will be perfectly absorbed. We point out that PAC applies to elastic beam/plate-type structures composed of any conventional material with internal loss or additional damping. To intuitively display the absorption, based on the resonator parameter described in Fig. 1(e), we plot the reflection energy ratio $|R|^2$ of flexural waves, as shown in Fig. 1(f). The corresponding absorption coefficient $\alpha = 1-|R|^2$ is also added to Fig. 1(f), which shows a perfect absorption peak.

Due to $\varsigma$ equals $\Gamma_{\text{rad}}$, the corresponding quality factor of the loss $Q_{\text{loss}}$ equals $Q_{\text{rad}}$. The total quality factor of the resonator with perfect absorption can be expressed as

$$Q = \frac{Q_{\text{rad}}}{2}. \tag{12}$$

, where $\frac{1}{Q} = \frac{1}{Q_{\text{rad}}} + \frac{1}{Q_{\text{loss}}}$. Based on Eqs. (5), (7), and (12), $Q$ varying with $\gamma_{\text{rad}}$, for $n=1$ and $n=2$, are shown in Fig. 1(g), respectively. $Q$ of the perfect absorber decreases with the increase of $\gamma_{\text{rad}} = \varsigma$.

## 3. Lossy elastic beam

As a typical example, we investigate the non-Hermitian LEM composed of a lightweight waveguide resonator with variable thickness $d_2$, as shown in Fig. 2(a). For simplicity, the LEM has the same material of metal alloys with the background elastic beam of thickness $d_1$. Increasing the thickness ratio $\varepsilon_d = d_1/d_2$ can improve $Đ$ and $\kappa$ of the model to get $\arg(r_{11}) \approx \pi/2$, according to Eq. (S5). Therefore, when $\varepsilon_d$ is large enough to weaken the stiffness of the LEM (a large $Đ$), the real part of Pole $\text{Re}\left(\Omega_{\text{Pole}}^{\text{Lossless}}\right) = \varphi$ can be rewritten as

$$\text{Re}(k_2)\cdot L = \varphi \approx \frac{\pi}{2} + n\pi, \quad n \geq 1, \tag{13}$$

where $k_2 = \beta_2\sqrt{\omega}$. Eq. (13) describes the so-called $n^{\text{th}}$ Fabry-Pérot (FP) resonance in the elastic wave system. Importantly, sufficiently weak stiffness of resonator (thickness ratio) to make the reflected wave $r_{11}$ have a $\pi/2$ modified phase is the key to the FP resonance existence, which is different from that in optics and acoustics. Note that this $\pi/2$ modified phase can also be obtained by adjusting the material parameters of the resonator. The resonance frequency only depends on the length *L*. Here, we consider practical metal alloys or composite structures with small internal losses, described by the loss factor, which is often less than 0.1. The traditional idea is that it is impossible to achieve perfect absorption only through weak internal loss. However, based on the above-discussed loss-modulation non-Hermitian model, we break through this possibility. According to Eq. (11), the thickness ratio $\varepsilon_d$ is surprisingly reduced to a constant regarding to $\eta$

$$\varepsilon_d = \left( \frac{-\vartheta - \sqrt{\vartheta^2 + \psi_1(\vartheta)} + \sqrt{2\vartheta^2 + \psi_2(\vartheta)}}{4\vartheta + 8} \right)^2, \tag{14}$$

where $\vartheta$ is loss constant, $\vartheta = 2e^{-\kappa\eta}$, and $\kappa = (\pi + 2n\pi)/4$. $\psi_1$ and $\psi_2$ are univariate functions of $\vartheta$ (see detailed derivation in Appendix D). Interestingly, it indicates that perfect absorption only depends on modulating the stiffness of the resonator (thickness ratio) and loss factor, and does not rely on the length *L*. The modulating method opens a new way of designing elastic wave absorbers and makes the loss factor become an essential design degree of freedom. Note that the effective loss factor of the resonator can be flexibly modulated by additional external damping (Cao et al., 2020) for a wider design degree of freedom.

Based on Eqs. (13) and (14), once $\varepsilon_d$ and $\eta$ satisfy Eq. (14), the LEMs with different lengths can achieve perfect absorptions whose different resonance frequencies are decided by Eq. (13), as shown in Fig. 2(a). Fig. 2(b) shows the corresponding reflected phase spectrum. Two absorption spectrums with $\alpha$ approximating the unity at 600 Hz and 1000 Hz (labeled P1 and P2 in Fig. 2(a)) are shown in Fig. 2(c). The corresponding simulated results are consistent with these analytical ones. According to Eq. (13), the LEM has a subwavelength size described by the ratio $\ell$ of the resonator length to the peak absorption wavelength

$$\ell = \frac{1+2n}{4}\frac{k_1}{k_2} = \frac{1+2n}{4\sqrt{\varepsilon_d}} < \frac{1}{5}. \tag{15}$$

The subwavelength size indicates that the compact and lightweight absorber can be applied to a lower frequency than the conventional ones (Deng and Zheng, 2022; Gao et al., 2021; Kerwin, 1959; McCormick and Shepherd, 2019; Pelat et al., 2020; Sun et al., 1995; Tang et al., 2016).

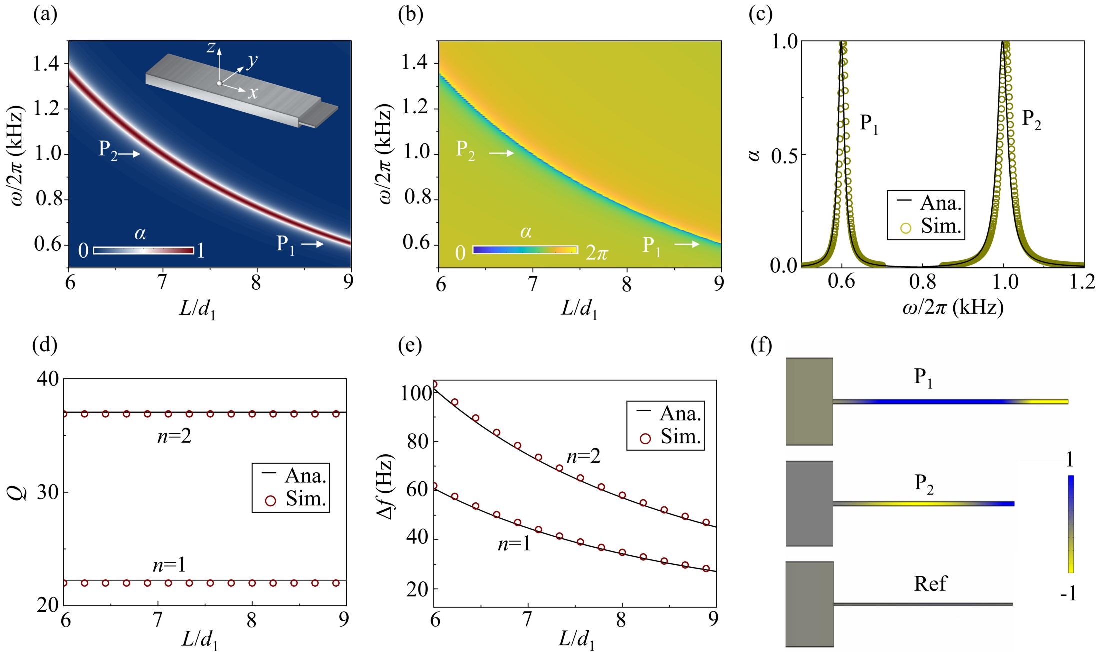

**Fig. 2.** Lossy elastic beam. (a) The map of absorption coefficient varying frequency and the length $L$ of the resonator. The model in the illustration is an elastic beam of the thickness $d_1$ 4.5 mm with the waveguide resonator of the thickness $d_2$ 0.3 mm. The model composed of Mn-Cu alloy has a width $b$ of 13 mm. (b) The map of the reflection phase. (c) Two absorption spectrums with $\alpha$ approximating one at 600 Hz and 1000 Hz (labeled P1 and P2 in Fig. (a)). (d) The quality factor $Q$ varies with $L$ for the absorber based on 1st and 2nd resonance, i.e., $n$=1 and 2 in Eq. (7). (e) The

resonance linewidth $\Delta f$ of the absorber is based on the 1st and 2nd resonance. (f) The simulated wavefields in the model labeled P1, the model labeled P2, and the reference model (Ref model).

Based on Eqs. (7) and (13), the $Q$ of the LEM based on $n^{\text{th}}$ resonance can be rewritten as

$$Q=\frac{\left(\pi+2n\pi\right)^{2}-4{\Gamma_{\text{rad}}}^{2}}{16\left(\pi+2n\pi\right)\Gamma_{\text{rad}}}. \tag{16}$$

We plot the $Q$ varying with $L$ for $n=1$ and $n=2$, respectively, as shown in Fig. 2(d). These analytical results of $Q$ are consistent with the simulated ones, which are independent of $L$. The reason is that $\Gamma_{\text{rad}}$ in Eq. (16) quantifies the radiative decay at the interface $\tilde{l}_1$ without considering the resonator length $L$. In addition, the linewidth of LEM at its half-maximum can be expressed as

$$\Delta f=\frac{2\cdot\text{Im}\left[(\Omega_{\text{Pole}}^{\text{Loss}})^{2}\right]}{2\pi}=\left(1+2n\right)\Gamma_{\text{rad}}\cdot\sqrt{\frac{\text{Re}\left(D_2\right)}{\rho_2 d_2 L^4}}. \tag{17}$$

According to Eq. (17), we plot $\Delta f$ for $n=1$ and $n=2$, respectively, as shown in Fig. 2(e). The linewidth decreases with the increase of $L$.

To further reveal the absorption mechanism of the LEM, we extract the amplitude fields in the models from simulations, as shown in Fig. 2(f). The energy densities of wavefields (labeled P1 and P2 in Fig. 2(a)) are greatly strengthened in the LEM due to the resonance with loss modulation, which enhances energy absorption. For comparison, when the thickness $d_2$ of the LEM is reduced to half to increase dissipative decay constant $\text{Im}\left(k_2\right)L$, but the loss-modulation PAC is not considered, the wavefields are not strengthened. The incident wave is hardly absorbed. It indicates that one key factor in obtaining the perfect absorption is significantly increasing the energy density of the resonator by judiciously harnessing the tailored losses.

## 4. Broadband absorption of LEM based on weak coupling

To realize broadband absorption, and inspired by the multi-resonance weak coupling theory for optic (Cui et al., 2012) and acoustic (Huang et al., 2019; Yang et al., 2017) absorbers, we have established the elastic wave counterpart with unique evanescent wave hybridization. As shown in Fig. 3(a), the LEM is composed of parallel resonators with different lengths at the background elastic beam boundary. The scattering equation of the non-Hermitian elastic beam system is

$$ {}^{b}\mathbf{G}_1 \cdot \begin{pmatrix} {}^{b}\mathbf{T}^{(\mathrm{I})} \\ {}^{b}\mathbf{T}_{\mathrm{L}}^{(\mathrm{II})} \\ {}^{b}\mathbf{T}^{(\mathrm{III})} \end{pmatrix} = {}^{b}\mathbf{G}_2, \tag{18} $$

where ${}^{b}\mathbf{T}^{(\mathrm{I})}$, ${}^{b}\mathbf{T}_{L}^{(\mathrm{II})}$, and ${}^{b}\mathbf{T}^{(\mathrm{III})}$ are scattering coefficient vectors. ${}^{b}\mathbf{G}_2$ is the coefficient vector of the incident wavefield and ${}^{b}\mathbf{G}_1$ is the parameter matrix coupling all lossy resonators. Eq. (18) comes from the degradation of Eq. (24) (see detailed derivation in Appendix F).

First, we design every resonator capable of generating perfect absorption for different frequencies. These resonators and the background beam form a non-coaxial structure with an offset $\Delta s$ , as shown in the illustration of Fig. 3(b). We show that the absorption map is independent of $\Delta s$, taking the center frequency of 1000 Hz as an example, as shown in Fig. 3(b). The independent proves that Eq. (14) based on the coaxial structure is still valid for these non-coaxial ones. The validity is due to the fact that the low-frequency flexural wave has the same deflection in the thickness direction of the thin plate. Based on Eq. (14), the absorption spectrum of each resonator is plotted by light grey curves in Fig. 3(c). All absorption peaks reach approximately the unity.

Further, as shown in Fig. 3(a), for example, the LEM is composed of ten resonators with different lengths $L$, which are $34.0\delta$, $33.6\delta$, $33.2\delta$, $32.8\delta$, $32.2\delta$, $31.7\delta$, $31.2\delta$, $30.4\delta$, $29.7\delta$, and $29.0\delta$ mm, respectively, $\delta=\left(1-\upsilon^2\right)^{\frac{1}{4}}$ is a constant. We point out that extending the elastic beam model infinitely in the y-direction will form a plate. The plane strain model of this plate has the same absorption spectrum as this elastic beam model (Cao et al., 2021c) if its resonator lengths become 34.0, 33.6, 33.2, 32.8, 32.2, 31.7, 31.2, 30.4, 29.7 and 29.0 mm, i.e., $\delta=1$.

Based on Eq. (18), we can get the analytical reflection coefficient of the LEM in the elastic beam, and the solid black line plots the absorption spectrum in Fig. 3(c). An average absorption coefficient higher than 0.8 in the frequency range from 851 Hz to 1196 Hz is obtained. Ten absorption peaks occur almost at the resonance frequencies of the resonators. It indicates that a weak coupling between resonators in the LEM induces broadband absorption. The simulated results, marked by circles in Fig. 3(c), are consistent with the analytical ones. We point out that all the results are not optimized, and the absorption effect of the LEM can be further improved by parameter optimization. On the other hand, increasing the number of resonators will increase the bandwidth. However, additional resonators will make the fabrication process of the specimen more difficult, which will limit the absorption bandwidth of the actual specimen. The non-local properties of the resonators (Díaz-Rubio et al., 2019; Zhou et al., 2021) may be an effective way to break this limit.

To gain insights concerning the ten absorption peaks, the corresponding amplitude, and energy flux fields (marked by the arrows in Figs. 3(d)-3(f)) in the model are obtained by simulations. Each amplitude field is highly concentrated to only one resonator when the excitation frequency approximates its resonance frequency. For example, the amplitude fields corresponding to three specific frequencies (labeled P3, P4, and P5 in Fig. 3(c)) are shown in Figs. 3(d)-3(f). These highly concentrated fields are a clear sign of the weak coupling between the resonators, leading to broadband absorption of the LEM.

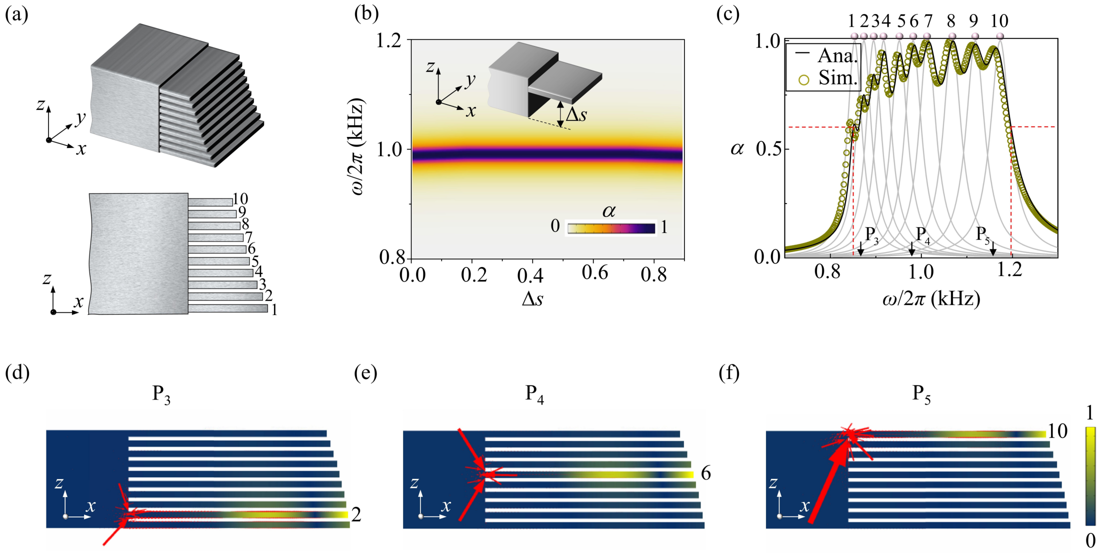

**Fig. 3.** Broadband absorption in an elastic beam. (a) Ten waveguide resonators with different lengths are connected in parallel to the background beam in the theoretical model. The host beam and resonators have the same thickness as the model in Fig. 2(a). These resonators are numbered in their cross-section of the *xy* plane. (b) The resonator and the background beam form a non-coaxial structure in the illustration. The simulated absorption spectrum varies with frequency and $\Delta s$ for the resonator with the center frequency of 1000 Hz. (c) The light grey curve plots the absorption spectra of every single resonator. The analytical and simulated absorption spectra of the LEM are plotted. (d)-(f) The simulated amplitude and energy flux fields for three specific frequencies (labeled P3, P4, and P5 in Fig. 3(c)).

## 5. Broadband and near-omnidirectional perfect absorption of the LEM in an elastic plate

Fig. 4(a) shows the theoretical model, $M$ different units consisting of gradient-length waveguides and lossy multi-resonators composed of $N$ resonators ($M=3$, $N=10$ in Fig. 4(a)). The multi-resonators are the same as the one presented in the theoretical model of section 2.3. These $M$ units are combined into a supercell with a width of $g$ at the boundary of the background plate, as shown in Fig. 4(a). Then, the supercell is periodically arrayed along the $y$-axis to form a gradient lossy elastic metasurface, which is uniformly defined as the LEM in the plate-type structure. Previous research [9] investigated multiple reflections of diffraction modes from the gradient elastic metasurface composed of a simple waveguide. Here, we introduce the loss modulation system to the classical metasurface to design the LEM, improving performance and expanding the degrees of design freedom. The multiple reflections enhance the energy dissipation from loss modulation to achieve broadband and near-omnidirectional perfect absorption of flexural waves in a plate-type structure. We establish a unified analytical model through modified mode coupling methods by the transfer matrix method.

In Fig. 4(a), the background plate, the gradient-length waveguides, and lossy multi-resonators are divided into region (I), region (II), and region (III) by the dotted lines $\tilde{l}_3$ and $\tilde{l}_4$. In region (I), the governing equation for the flexural waves in the two-dimension form is $D_1\left(\nabla^2\nabla^2+\rho_1 d_1\frac{\partial^2}{\partial t^2}\right)w^{(\mathrm{I})}(x,y,t)=0$, where $\nabla^2=\frac{\partial^2}{\partial x^2}+\frac{\partial^2}{\partial y^2}$. The displacement field, including all diffraction modes in region (I), can be expressed as

$$w^{(\mathrm{I})}(x,y)=\sum_{j=0}^{\pm\infty}(\delta_{j,0}\cdot e^{-\mathrm{i}k_{y0}\cdot y}e^{-\mathrm{i}k_{x0}\cdot x}+\Re_j e^{-\mathrm{i}k_{yj}\cdot y}e^{\mathrm{i}k_{xj}\cdot x}+\tilde{\Re}_j e^{-\mathrm{i}k_{yj}\cdot y}e^{\hat{k}_{xj}\cdot x}), \tag{19}$$

where $\delta_{n,0}$ is the Kronecker delta, $\Re_j$ and $\tilde{\Re}_j$ are the reflection amplitudes of $j^{\text{th}}$ order propagating and $j^{\text{th}}$ order evanescent diffraction modes, respectively. The number of propagation diffraction modes in the background structure can be decided by (Cao et al., 2020)

$$J=2\hat{J}+1=2\cdot\text{roundup}\left(2k_0/\gamma\right)-1, \tag{20}$$

where $\gamma=2\pi/g$ is the reciprocal lattice vector along the metasurface. $k_{xj}=\sqrt{k_1^{\ 2}-k_{yj}^{\ 2}}$ and $\hat{k}_{xj}=-\mathrm{i}\sqrt{-k_1^{\ 2}-k_{yj}^{\ 2}}$ are $x$-component wave vectors of the propagation and evanescent flexural wave diffraction modes, respectively. The coefficient vector of the reflection diffraction field can be defined as $\mathbf{T}^{(\mathrm{I})}=\left[\mathbf{e}_1,\cdots\mathbf{e}_j,\cdots\mathbf{e}_J\right]^{\mathrm{T}}$, where $\mathbf{e}_j=\left[\Re_j,\tilde{\Re}_j\right]^{\mathrm{T}}$.

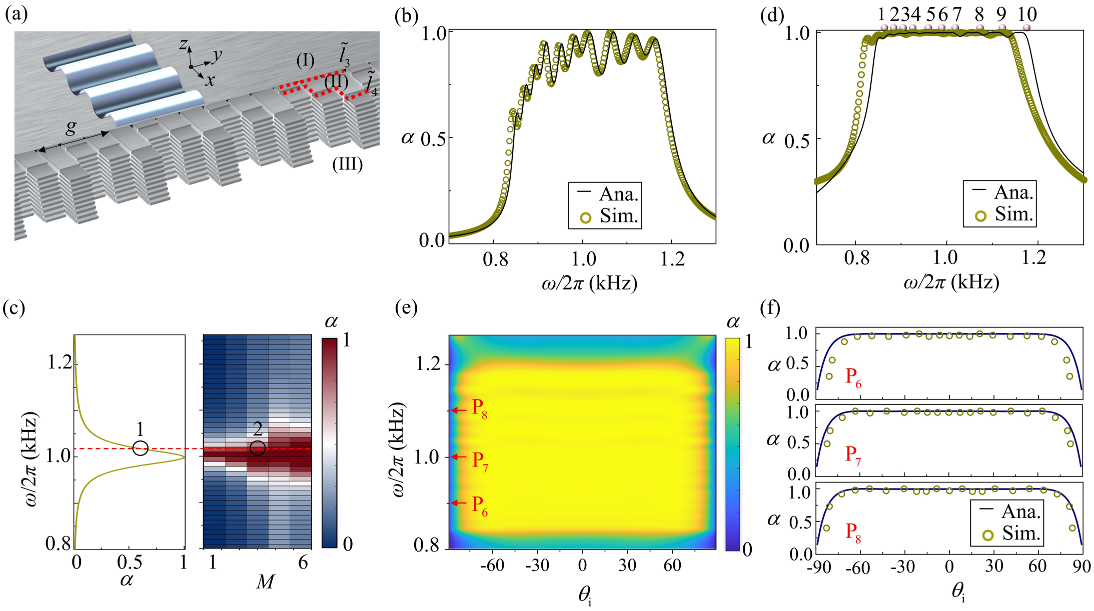

**Fig. 4.** Broadband and near-omnidirectional absorption in an elastic plate. (a) Schematic diagram of the theoretical LEM model in the plate-type structure. The thicknesses of gradient-length waveguides are the same as that of the background plate, i.e., 4.5 mm. The widths of the supercell $g$ and subunit $b$ are 40.6 mm and 13 mm, respectively. (b) The absorption spectrum of the model without gradient waveguides ($M=1$ and $N=10$). (c) The absorption spectrum of the single resonator ($M=1$ and $N=1$) with the resonance frequency of 1000 Hz in the left subgraph. The

absorption coefficient of the theoretical model with $N = 1$ varying with frequency and unit number *M*. (d) The absorption spectrum of the theoretical model with $M = 3$ and $N = 10$. (e) The map of the absorption coefficient of the theoretical model with $M = 3$ and $N = 10$ varying with the frequency and the incident angle. (f) The corresponding simulated and analytical absorption coefficients for three frequencies of 900, 1000, and 1100 Hz.

In region (II) of one supercell, since the width of the subunit is much smaller than the operating wavelength, only the fundamental mode needs to be considered. The displacement of flexural waves in the *m*th waveguide can be expressed as

$$w_m^{(\mathrm{II})}(x) = a_m e^{-\mathrm{i}k_1 \cdot x} + b_m e^{-k_1 \cdot x} + c_m e^{\mathrm{i}k_1 \cdot x} + d_m e^{k_1 \cdot x}, \tag{21}$$

where $a_m$, $b_m$, $c_m$, and $d_m$ are the amplitude coefficients of the fundamental mode at the left interface of the region (II). The coefficient vector can be defined as $\mathbf{T}^{(\mathrm{II})} = \left[\mathbf{k}_1, \cdots \mathbf{k}_m, \cdots \mathbf{k}_M\right]^{\mathrm{T}}$, where $\mathbf{k}_m = \left[a_m,\ b_m,\ c_m,\ d_m\right]^{\mathrm{T}}$. In the region (III), considering the right free boundary of the multi-resonator, the displacement in the *n*th resonator on the edges of the *m*th waveguide can be expressed as

$$\begin{aligned} w^{(\mathrm{III})} = & \left[ e^{-\mathrm{i}k_n \cdot x} - \mathrm{i}e^{-2\mathrm{i}k_n \cdot L_n + \mathrm{i}k_n \cdot x} + (1-\mathrm{i}) e^{-(\mathrm{i}+1) \cdot k_n L_n + k_n \cdot x} \right] \hat{a}_{mn} \\ & + \left[ e^{-k_n \cdot x} + \mathrm{i}e^{-2k_n \cdot L_n + k_n \cdot x} + (1+\mathrm{i}) e^{-(\mathrm{i}+1) k_n \cdot L_n + \mathrm{i}k_n \cdot x} \right] \hat{b}_{mn}, \end{aligned} \tag{22}$$

where $\hat{a}_{mn}$ and $\hat{b}_{mn}$ are the amplitude coefficients at the left interface of the resonator. $L_n$ is the length of the resonator. The coefficient vector can be defined as

$$\mathbf{T}^{(\mathrm{III})} = \begin{bmatrix} \mathbf{G}_1 \\ \vdots \\ \mathbf{G}_m \\ \vdots \\ \mathbf{G}_M \end{bmatrix}, \quad \mathbf{G}_m = \begin{bmatrix} \mathbf{g}_{m1} \\ \vdots \\ \mathbf{g}_{mn} \\ \vdots \\ \mathbf{g}_{mN} \end{bmatrix}, \quad \mathbf{g}_{mn} = \begin{bmatrix} \hat{a}_{mn} \\ \hat{b}_{mn} \end{bmatrix}, \tag{23}$$

According to the continuous boundary and orthogonality conditions, based on modified mode coupling methods, the scattering equation in the non-Hermitian elastic plate system can be derived as (see detailed derivation in Appendix E)

$$\mathbf{G}_1 \cdot \begin{pmatrix} \mathbf{T}^{(\mathrm{I})} \\ \mathbf{T}_{\mathrm{L}}^{(\mathrm{II})} \\ \mathbf{T}^{(\mathrm{III})} \end{pmatrix} = \mathbf{G}_2, \tag{24}$$

where $\mathbf{G}_1$ is a square matrix of size $(2J+4M+2MN)\times(2J+4M+2MN)$, and $\mathbf{G}_2$ is a column vector of size $(2J+4M+2MN)$. Eq. (24) can accurately calculate the response of all diffraction modes in the background structure.

When the reciprocal lattice vector $\gamma$ of the metasurface is greater than $2k_1$, there is only 0th propagation diffraction mode in the background plate, according to Eq. (20). The mode has the maximum number $E$ of multiple reflections due to phase shift matching at the interface. The maximum number $E$ equals subunit number $M$ in one supercell (Cao et al., 2020). The absorption coefficient of the LEM can be defined as $\alpha = 1-|\Re_0|^2$, where $\Re_0$ is the amplitudes of 0th propagation diffraction mode in the background structure. When there is no gradient for the LEM, i.e., $M=1$ and $N=10$ in the model, the absorption spectrum of LEM in the plate model is almost consistent with that in the multi-resonators beam model, as shown in Fig. 4(b).

To quantitatively analyze the enhancement effect of multiple reflections on absorption, we replace the multi-resonator in Fig. 4(a) with a single resonator, i.e., $N=1$. The absorption spectrum of the single resonator ($M=1$, $N=1$) with the resonance frequency of 1000 Hz is shown in the left subgraph of Fig. 4(c). The corresponding absorption coefficient $\alpha$ varying with frequency and $M$ can be obtained by Eq. (24). The absorption spectrum is shown in the right subgraph of Fig. 4(c). When $M$ increases, the frequency band with an absorption coefficient of approximately one (width of the magenta area in the $y$-direction) is gradually enlarged. For example, for the frequency marked by the red dotted line, the absorption coefficient of the single resonator is about 0.6 (marked by circle 1). The absorption coefficient of the LEM increases with $M$ and reaches almost 0.95 when $M=3$ (marked by circle 2).

Therefore, we choose $M=3$ to design the LEM, which can have a high absorption performance and increase the absorption coefficient of the single resonator from 0.6 to close to 1. As shown in Fig. 4(a), the lengths of three gradient-length waveguides can be calculated by $S_i=(i-1)\cdot\lambda_{f_0}/(2M)+\tilde{L},\ i\in 1\cdots M$ . $\tilde{L}$ is the additional length constant. $\lambda_{f_0}$ is the wavelength of flexural waves in the host plate in the frequency of $f_0=1000\text{ Hz}$. The absorption spectrum of LEM has broad absorption, as shown in Fig. 4(d). All absorption peaks in Fig. 4(b) are increased and reach almost one, i.e., broadband perfect absorption. The simulated results present an excellent agreement with the analytical ones. Further, based on Eqs. (24), we analytically solve the absorption coefficient varying with incident angle and frequency. The high absorption coefficient (exceeds 0.8) occurs in the frequency range from 836 to 1194 Hz, and for the angle ranging from −81° to 81°, as shown in Fig. 4(e). We define the high-performance absorption for the angle ranging from −90° to 90° as omnidirectional absorption. Therefore, the proposed LEM has high performance and achieves almost omnidirectional absorption, i.e., near-omnidirectional absorption.

We have compared the corresponding simulation results with the analytical ones for three different frequencies, 900, 1000, and 1100 Hz (labeled P6, P7, and P8 in Fig. 4(e)). An excellent agreement is obtained, as shown in Fig. 4(f). The near-omnidirectional perfect absorption stems from interface impedance matching in a wide range of incident angles due to two points. The first is the high phase resolution of the LEM with a deep subwavelength unit width. The second is that flexural evanescent waves (Liu et al., 2017) compensate for the impedance mismatch of the interface $\tilde{l}_1$.

## 6. Asymmetrical perfect absorption at the exceptional point

To investigate the exceptional point (EP), we have designed the non-Hermitian elastic metamaterial described in section 5 as a two-port system, as shown in Fig. 5. The scattering waves in the left and right ports have complex displacement amplitudes $w_{1-}$, $w_{1+}$, and $w_{2-}$, $w_{2+}$, respectively. The subscripts 1 and 2 indicate the left and right ports, and the subscripts + and – represent incidence and reflection in the two ports, respectively. The scattering equation of the two-port system can be expressed as

$$\mathbf{w}_- = \boldsymbol{\psi} \cdot \mathbf{w}_+, \tag{25}$$

where $\mathbf{w}_- = \left[w_{2-}, w_{1-}\right]^T$ and $\mathbf{w}_+ = \left[w_{1+}, w_{2+}\right]^T$ are scattering vectors. The scattering matrix $\boldsymbol{\psi}$ connects the incidences and reflections in the two ports. We should point out that the idea of this model comes from acoustics (Wang et al., 2019), but it is implemented in challenging elastic waves with different loss systems. This section shows that our model has generalizability to the study of non-Hermitian elastic wave systems.

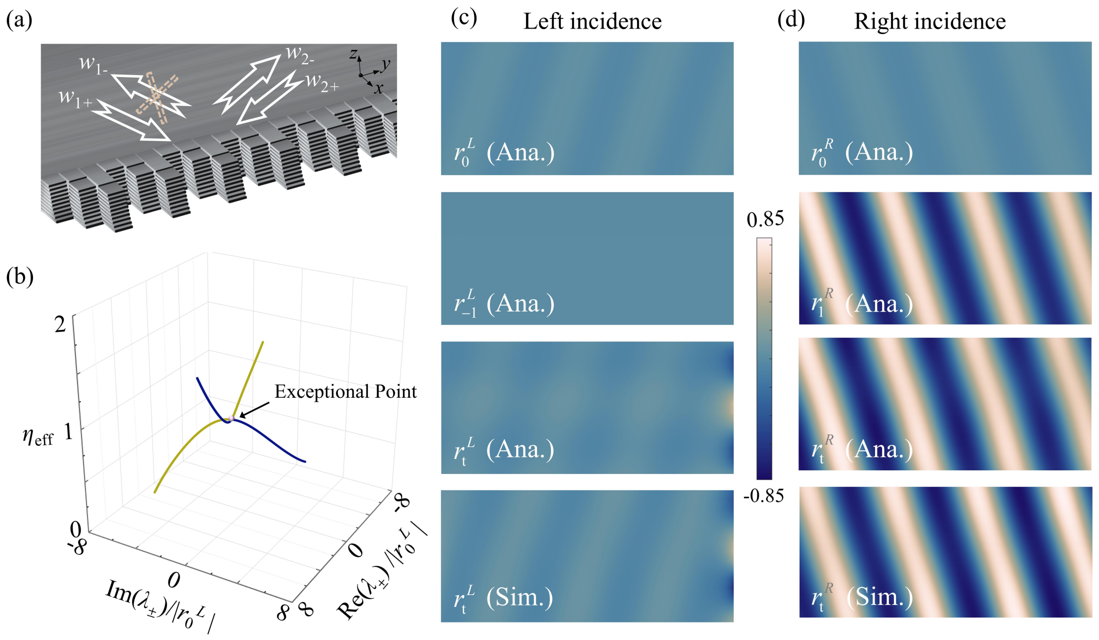

Fig. 5 Asymmetrical perfect absorption. (a) a two-port system in the non-Hermitian elastic metamaterial. (b) The trajectories of the eigenvalues of the scattering matrix vary with the loss $\eta_{\text{eff}}$. (c) and (d) The reflected wavefield at the EP for the left and right incidences, respectively.

Without loss of generality, we set the incidence angles as +30° and -30° for left and right incidences, respectively. Based on Eq. (20), the reciprocal lattice vector $\gamma = 2\pi/g = k_0$ can satisfy only two propagation diffraction modes existing while others are evanescent for both incidences. Recalling the diffraction theorem

$$k_{yn} = k_y^{\text{in}} + j\gamma, \tag{26}$$

where $k_y^{\text{in}}{=}k_0 \sin\theta_{\text{in}}$ and $k_{yj}{=}k_0 \sin\theta_{\text{r}}^j$ mean $y$-component wave vectors of the incident waves and $j^{\text{th}}$ order diffraction, respectively. According to Eq. (26), for the left incidence $w_{1+}$ of $\theta_{\text{in}} = 30^{\circ}$, only the $0^{\text{th}}$ and $-1^{\text{st}}$ order diffraction modes can propagate, corresponding to the specular reflection of $\theta_{\text{r}} = 30^{\circ}$ and retroreflection of $\theta_{\text{r}} = -30^{\circ}$, respectively. For the right incidence $w_{2+}$ of $\theta_{\text{in}} = -30^{\circ}$, only the $0^{\text{th}}$ and $1^{\text{st}}$ order diffraction modes are propagation ones, representing the specular reflection of

$\theta_{\mathrm{r}} = -30^{\mathrm{o}}$ and retroreflection of $\theta_{\mathrm{r}} = 30^{\mathrm{o}}$, respectively. Therefore, the scattering matrix $\boldsymbol{\psi}$ can be obtained as

$$\boldsymbol{\psi} = \begin{bmatrix} r_0^L & r_1^R \\ r_{-1}^L & r_0^R \end{bmatrix}, \tag{27}$$

where $r$ is the reflection coefficient of the corresponding diffraction mode. The subscripts of $r$ indicate the diffraction order $j$, and the superscripts $L$ and $R$ indicate the left and right incidences, respectively. Based on the established analytical model described by Eq. (24), we can accurately obtain the reflection spectra of all diffraction modes. Owing to reciprocity, specular reflections from both sides are identical, i.e., $r_0^L = r_0^R$. However, the extraordinary reflections $r_{-1}^L$ and $r_1^R$ are different.

For simplicity, the resonator number in one subunit is set to 1, i.e., $N = 1$ in Eq. (24). All resonators are the same. We modulate the losses of the resonators simultaneously, which are characterized by an equivalent loss factor $\eta_{\mathrm{eff}}$. The background plate and the gradient-length waveguides are considered small structural losses $\eta_0$. Based on Eq. (24), we choose unit number $M$=20 to maximize the retroreflection efficiency by optimization. The operating frequency is 2340 Hz. The additional length constant $\tilde{L}$, the resonator length, and the resonator thickness are modified to 31.14, 12.46, and 0.47 mm, respectively. Other geometric and material parameters remain the same as section 5. The eigenvalues $\lambda_{\pm} = r_0^L \pm \sqrt{r_{-1}^L \cdot r_1^R}$ of the scattering matrix are calculated by Eq. (24). Their trajectories vary with the loss $\eta_{\mathrm{eff}}$, as shown in Fig. 5(b). At the EP where $\eta_{\mathrm{eff}} = 0.93$, the two eigenvalues $\lambda_{\pm}$ coalesce together with the same eigenvectors $\mathbf{v}_{\pm} = \left[1,\ 0\right]^T$. The same eigenvectors show that the initially orthogonal eigenvectors become parallel, which directly demonstrates the EP from the non-Hermiticity of the elastic wave system (Wang et al., 2019).

We theoretically calculate the reflected wavefield $\mathrm{Re}\left[w_{\mathrm{r}}(x,y)\right]$ at the EP by Eqs. (19) and (24). Figs. 5(c) and 5(d) illustrate the reflected wavefields for the left and right incidences, respectively. In the eight subgraphs from top to bottom, the first, second, third, and fourth rows of subgraphs show the analytical specular reflection fields from 0th diffractions, the analytical retroreflection fields from 1st or -1st diffractions, the analytical total fields from all diffraction modes, and the simulated total fields, respectively. Due to reciprocity, specular reflections show a symmetrical pattern while strongly suppressed to enhance the overall asymmetric, as shown in the first row of subgraphs. The second row of subgraphs demonstrates the asymmetrical perfect absorption where no retroreflection $\left|r_{-1}^{L}\right|=0$ occurs for the left incidence and a strong retroreflection $\left|r_{1}^{R}\right|=0.85$ is present for the right incidence. The third row of subgraphs manifests the EP of the system. Compared to the right incidence with strong reflection, the waves are almost perfectly absorbed for the left incidence. To validate the theory, we have carried out the corresponding numerical simulations, and show the results in the fourth row of subgraphs. Good agreement between the simulated and analytical results confirms the correctness of the theoretical model.

## 7. Experimental verification of theoretical models

Our proposed design method is universal and applicable to almost all solid beam/plate-type structures composed of any material (see absorption spectrums of

LEMs in elastic beams with different materials of concrete, cross-grain wood, plexiglass (PMMA), and Aluminum alloy, in Appendix J). We should point out that the proposed theoretical approach is valid for both the low and high-frequency ranges, verified by the corresponding numerical simulations. The size of the designed specimens for the high-frequency range is relatively small, which can facilitate specimen printing by the 3D printer and attaching the blue-tack layer in the boundary to design a non-reflection boundary (Cao et al., 2021c). Therefore, we have verified the proposed theory through experiments in the high-frequency range.

To verify the universality and facilitate specimen processing, we have chosen a 3D printer to fabricate three types of specimens with PLA material, which verify the design model in section 3, section 4, and section 5, as shown in the illustration of Figs. 6(e), 6(g), and 6(i), respectively. They are named as the single resonator specimen (an elastic beam with one resonator), the multi-resonators specimen (an elastic beam with multi-resonators), and the designed plate specimen, respectively. Fig. 6(a) shows the experiment setup. The absorption spectrum can be measured using the measurement mode "FFT" of Polytec Scanning Vibrometer 500 (PSV-500).

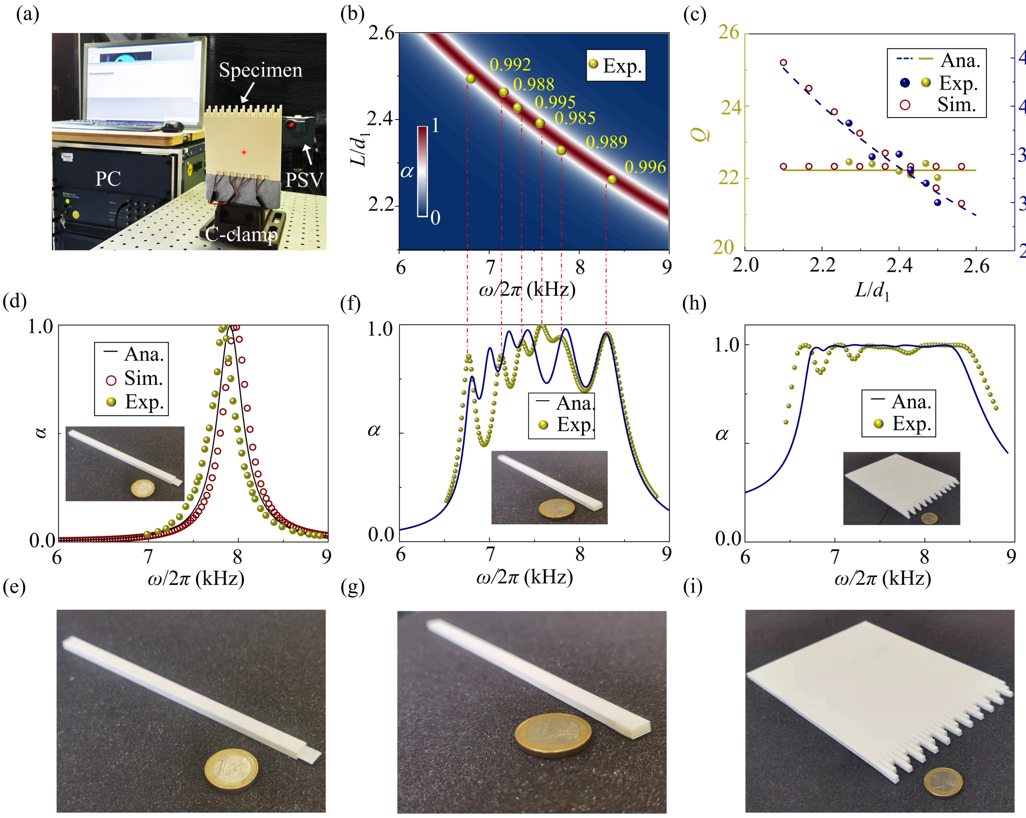

Fig. 6 Experimental verification of theoretical models. (a) The experiment setup. (b) For the single resonator specimen, the map of the analytical absorption coefficient varying with the frequency and the $L$. Six points corresponding to these measured absorption coefficients are added. (c) The map of Q and $\Delta f$ of the absorption spectrum varying with $L$, calculated by Eqs. (16) and (17), respectively. The corresponding results obtained from these measured absorption spectrums are added. (d) The experimental absorption spectrum and the analytical one for the 2nd single resonator specimen. (e) The printed single resonator specimen with PLA material. (f) For the multi-resonators specimen, the analytical and measured absorption spectrums are shown. (g) The printed multi-resonators specimen with PLA material. (h) The experimental absorption spectrum and the analytical one of the designed plate specimen. (i) The printed plate specimen with PLA material.

First, we calculate the absorption coefficient of the single resonator specimen varying with frequency and the $L$ by the theoretical model. The map of absorption coefficients is shown in Fig. 6(b). The Q and $\Delta f$ of the absorption spectrum varying with $L$ are also calculated by Eqs. (16) and (17), respectively. The results are shown by the solid line and dotted line in Fig. 6(c), respectively, which have a good agreement with the simulated results. We have printed six single resonator specimens with different $L$ and measured their absorption spectrums, respectively (see detailed experimental measurements in Appendix H). Specific geometric parameters of resonators in the six single resonator specimens can be found in Appendix I. Six points regarding the length of these specimens and the frequency of the corresponding absorption peak are added to Fig. 6(b). The corresponding absorption coefficients are marked on the right of these points. These coefficients reach approximately one, which means the flexural waves are almost completely absorbed. In addition, the Q and $\Delta f$ obtained from these measured absorption spectrums are added to Fig. 6(c). The experimental results are in good agreement with the theoretical model results, although some minor deviations due to the manufacturing error of the specimen are observed.

Fig. 6(d) also shows the agreement between the experimental absorption spectrum and the analytical and simulated ones for the 2nd single resonator specimen. The measured absorption peak is 0.989, as shown in Fig. 6(b). To illustrate the absorption intuitively, we have realized the dynamic full wavefield in the single resonator specimen at the resonance frequency of 7.84 kHz by the "time" measurement mode (see Videos S1, Supplementary materials). The incident wave is not reflected when it enters the LEM, which means that it, indeed, perfectly absorbs flexural waves. In addition, the displacement deformations inside the LEM are greatly enhanced, which confirms that the loss modulation significantly increases energy density. For comparison, we have also measured the dynamic full wavefield at 9 kHz, away from the central frequency. The measured result is presented in Videos S2, Supplementary materials, which shows that the wavefield is a standing wave, and the displacement deformation inside the resonator is not enhanced.

To verify the broadband absorption of LEM based on weak coupling, we print the multi-resonators specimen, i.e., an elastic beam with multi-resonators, as shown in Fig. 6(g). The LEM in the multi-resonators specimen consists of six resonators with different $L$. For experimental consistency, the six resonators are the same as those in six single resonator specimens in Fig. 6(b). The analytical absorption spectrum of the multi-resonators specimen, which is calculated by the theoretical model described by Eq. (18), is shown by the solid line in Fig. 6(f). The measured absorption spectrum is added by solid dots to Fig. 6(f). We can see some relatively large deviations, which is due to the amplification of the manufacturing error by the coupling between resonators. However, we can still find that the number of absorption peaks is consistent. More importantly, the frequencies of these peaks are consistent with the resonance frequencies of the six single resonators, described by six points in Fig. 6(b). To intuitively show their connection, we connect these peaks in Fig. 6(b) to the points in Fig. 6(f) by red dotted lines. They are one-to-one correspondence. The correspondence confirms that the broadband absorption of the LEM is from the coupling between the six resonators.

To verify the broadband absorption of the LEM in the plate-type structure, we print the designed plate specimen with PLA material, as shown in Fig. 6(i). The designed plate specimen is consistent with the model in Fig. 4(a), but it has fewer resonators to verify universality and simplify specimen processing, i.e., $M = 3$ and

$N = 6$. Specific geometric parameters of the plate specimen can be found in Appendix I. For experimental consistency, the dimensions of the six resonators in the designed plate specimen are the same as the ones in the multi-resonators specimen in Fig. 6(g). Solid dots show the measured absorption spectrum of the designed plate specimen in Fig. 6(h). It shows a high-efficiency average absorption ($\alpha > 0.8$) in frequencies ranging from 6.72kHz to 8.42 kHz. The measured results are in good agreement with the theoretical ones based on Eq. (24). Some small observed deviations come mainly from the manufacturing error of the specimen and the imperfect excitation signal. Compared with the absorption spectrum in Fig. 6(f), all absorption peaks reach one, and the curve is approximately a flat band. This confirms the broadband perfect absorption of the LEM in the plate-type structure.

## 8. Discussion and conclusion

We have established a theoretical model to design the subwavelength lightweight lossy elastic metamaterials in a non-Hermitian elastic beam or plate system, which can provide a general way of breaking through the challenges of broadband vibration absorption in low frequency. We have numerically and experimentally verified the effectiveness of the theoretical method in elastic beam/plate-type structures.

In acoustics, significant progress has been made in the low-frequency perfect absorption of sound waves (Ma et al., 2014; Mei et al., 2012). However, it is no longer adequate for low-frequency noise over 120 dB caused by mechanical vibrations (Li et al., 2021a). Our approach has the potential to solve this challenge by absorbing vibrational energy to suppress the sound emission. In addition, the lossy elastic metamaterial can contain no additional damping material. It could open real possibilities in the families of the elastic metamaterial to realize absorption in extreme and harsh environments of high (or low) temperature and corrosion (Cao et al., 2021b). More than that, this work, in essence, paves the way for investigating loss-engineered wave scattering manipulation in elastic beam/plate-type structures, not limited to the dissipation-radiation-balance required by perfect absorption.

## Conflict of Interest

All authors declare that they have no conflict of interest.

## Supplementary materials

Video S1: The dynamic full wavefield in the 2nd single resonator specimen at the central frequency of 7.84 kHz measured by PSV-500.

Video S2: The dynamic full wavefield in the 2nd single resonator specimen at 9 kHz (away from the central frequency) measured by PSV-500.

## Appendix A. Analytical expression of the scattering matrix at the interface $\tilde{l}_1$

As shown in Fig. 1(b), the background elastic beam and the waveguide resonator are divided into region 1 and region 2 by the interface $\tilde{l}_1$. The general solution of displacement for the fourth-order partial derivative governing equation of flexural waves is

$$w_j(x,t)=\left(A_j e^{-\mathrm{i}k_j x}+B_j e^{\mathrm{i}k_j x}+C_j e^{-k_j x}+D_j e^{k_j x}\right)e^{\mathrm{i}\omega t}, \tag{A1}$$

where $j=1,2$ represent region 1 and region 2, respectively. *A*, *B*, *C*, and *D* are complex coefficients. $A_j e^{-\mathrm{i}k_j x}$ and $B_j e^{\mathrm{i}k_j x}$ correspond to the positive-going and negative-going propagating flexural waves, whereas $C_j e^{-k_j x}$ and $D_j e^{k_j x}$ correspond to the positive-going and negative-going evanescent flexural waves. The flexural wavenumber is $k=\beta\sqrt{\omega}$, where $\beta$ is the propagation constant, $\beta^4=\rho d/D$, and $D=d^3E/12$ is the flexural rigidity. *E* is the Young modulus, $\rho$ is density.

We make an incident positive-going flexural wave of $1\cdot e^{\mathrm{i}\omega t}$ at the left side of the interface $\tilde{l}_1$, so the wave fields at the left and the right sides of the interface $\tilde{l}_1$ can be expressed as follows:

$$\begin{cases} w_{\mathrm{L}}(x,t)=\left(1+r_{11}+r_{1\tilde{1}}\right)e^{\mathrm{i}\omega t} \\ w_{\mathrm{R}}(x,t)=\left(t_{12}+t_{1\tilde{2}}\right)e^{\mathrm{i}\omega t} \end{cases}, \tag{A2}$$

where the symbols *t* and *r* denote the transmission and reflection complex coefficients, respectively. The subscript ~ represents an evanescent flexural wave. 1 and 2 represent region 1 and region 2, respectively. The subscripts 11 and $1\tilde{1}$ represent the propagating reflection wave and evanescent one from the interface to region 1, respectively. The subscripts 12 and $1\tilde{2}$ represent the propagating transmission wave and evanescent one from the interface to region 2, respectively. Therefore, the vectors $\mathbf{k}_{\mathrm{L}}$ and $\mathbf{k}_{\mathrm{R}}$ for both sides of the interface can be written as:

$$\begin{cases} \mathbf{k}_{\mathrm{L}} = \begin{bmatrix} 1 & r_{11} & 0 & r_{1\tilde{1}} \end{bmatrix}^{\mathrm{T}} \\ \mathbf{k}_{\mathrm{R}} = \begin{bmatrix} t_{12} & 0 & t_{1\tilde{2}} & 0 \end{bmatrix}^{\mathrm{T}} \end{cases}. \tag{A3}$$

At the interfaces, the boundary conditions of displacement, slope, bending moment, and shear force must be satisfied (Cao et al., 2021a). According to these boundary conditions, we obtain the propagation equation

$$\mathbf{k}_{\mathrm{R}} = N_1 \mathbf{k}_{\mathrm{L}}, \tag{A4}$$

where $N_1$ is the transfer matrix. From Eq. (A4), we can obtain

$$r_{11} = \frac{2Đ\kappa\left(\kappa^2 - 1\right) - \mathrm{i}\left(1 - Đ\kappa^2\right)^2}{2Đ\kappa\left(1+\kappa^2\right) + \left(1+Đ\kappa^2\right)^2}, \tag{A5}$$

$$t_{12} = \frac{2(\kappa+1)(Đ\kappa^2+1)}{\kappa\left(Đ^2\kappa^4 + 2Đ\kappa^3 + 2Đ\kappa^2 + 2Đ\kappa + 1\right)}, \tag{A6}$$

where $Đ = \frac{D_1}{D_2}$ and $\kappa = \frac{k_1}{k_2}$. $D$ and $k$ are flexural stiffness and wavenumber of flexural waves.

In the same way, we make an incident negative-going flexural wave of $1 \cdot e^{\mathrm{i}\omega t}$ at the right side of the interface $\tilde{l}_1$, the vectors $\mathbf{k}_{\mathrm{L}}$ and $\mathbf{k}_{\mathrm{R}}$ for both sides of the interface can be rewritten as

$$\begin{cases} \mathbf{k}_{\mathrm{L}} = \begin{bmatrix} t_{21} & 0 & t_{2\tilde{1}} & 0 \end{bmatrix}^{\mathrm{T}} \\ \mathbf{k}_{\mathrm{R}} = \begin{bmatrix} 1 & r_{22} & 0 & r_{2\tilde{2}} \end{bmatrix}^{\mathrm{T}} \end{cases}. \tag{A7}$$

According to boundary conditions, we obtain the propagation equation

$$\mathbf{k}_{\mathrm{L}} = N_2 \mathbf{k}_{\mathrm{R}}. \tag{A8}$$

According to Eq. (A8), we can obtain

$$r_{22}=\frac{-2Đ\kappa\left(1-\kappa^{2}\right)-\mathrm{i}\left(1-Đ\kappa^{2}\right)^{2}}{2Đ\kappa\left(1+\kappa^{2}\right)+\left(1+Đ\kappa^{2}\right)^{2}} \tag{A9}$$

$$t_{21}=\frac{2Đ\kappa^{2}(\kappa+1)(1+Đ\kappa^{2})}{Đ^{2}\kappa^{4}+2Đ\kappa+2Đ\kappa^{2}+2Đ\kappa^{3}+1}. \tag{A10}$$

In the same way, we make an incident evanescent flexural wave of $1\cdot e^{\mathrm{i}\omega t}$ at the left and right sides of the interface $\tilde{l}_1$, and obtain the coefficients of $r_{\tilde{1}1}$, $r_{\tilde{1}\tilde{1}}$, $t_{\tilde{1}2}$, $t_{\tilde{1}\tilde{2}}$, $r_{\tilde{2}2}$, $r_{\tilde{2}\tilde{2}}$, $t_{\tilde{2}1}$, and $t_{\tilde{2}\tilde{1}}$, respectively.

The interface $\tilde{l}_1$ scatters incoming propagation waves with amplitudes $s_{1+}$, $s_{2+}$, incoming evanescent ones with amplitudes $\tilde{s}_{1+}$, $\tilde{s}_{2+}$, outgoing propagation ones with amplitudes $s_{1-}$, $s_{2-}$, and outgoing evanescent ones with amplitudes $\tilde{s}_{1-}$, $\tilde{s}_{2-}$. respectively. Therefore, we can obtain the scattering equation at the interface $\tilde{l}_1$:

$$\mathbf{S}^{-}=\begin{pmatrix} t_{12} & r_{22} & t_{\tilde{1}2} & r_{\tilde{2}2} \\ r_{11} & t_{21} & r_{\tilde{1}1} & t_{\tilde{2}1} \\ t_{1\tilde{2}} & r_{2\tilde{2}} & t_{\tilde{1}\tilde{2}} & r_{\tilde{2}\tilde{2}} \\ r_{1\tilde{1}} & t_{2\tilde{1}} & r_{\tilde{1}\tilde{1}} & t_{\tilde{2}\tilde{1}} \end{pmatrix}\mathbf{S}^{+}=\mathbf{M}_{\mathrm{I}}\cdot\mathbf{S}^{+}, \tag{A11}$$

where $\mathbf{S}^{-}=\left[s_{2-},s_{1-},\tilde{s}_{2-},\tilde{s}_{1-}\right]^{T}$ and $\mathbf{S}^{+}=\left[s_{1+},s_{2+},\tilde{s}_{1+},\tilde{s}_{2+}\right]^{T}$. $\mathbf{M}_{\mathrm{I}}$ is the scattering matrix of the interface. Eqs. (A1)-( are valid for a Kirchhoff plate when the propagation constant $\beta$ changes from $\beta^{4}=\rho d/D$ to $\beta^{4}=\rho d\big/\left[D\left(1-\upsilon^{2}\right)\right]$.

## Appendix B. The wavenumbers of Zero and Pole

The eigenvalue of the one-port elastic wave system equals the magnitude of the complex reflection coefficient, i.e., $\lambda_s=\left|R\right|$. Substituting a dimensionless complex wavenumber $\Omega=k_2L=\left(\tilde{k}_{\mathrm{RE}}+\tilde{k}_{\mathrm{IM}}\mathrm{i}\right)L$ into Eq. (3),

$$\lambda_s = \left| r_{11} + \frac{t_{12}t_{21}e^{-i\left[2\left(\tilde{k}_{\mathrm{RE}}+\tilde{k}_{\mathrm{IM}}\mathrm{i}\right)L-3\pi/2\right]}}{1-r_{22}e^{-i\left[2\left(\tilde{k}_{\mathrm{RE}}+\tilde{k}_{\mathrm{IM}}\mathrm{i}\right)L-3\pi/2\right]}} \right|. \tag{B1}$$

Simplifying Eq. (B1), we get

$$\lambda_s = \left| r_{11} + \frac{t_{12}t_{21}\left(\cos\tilde{\phi}-\mathrm{i}\cdot\sin\tilde{\phi}\right)e^{2L\cdot\tilde{k}_{\mathrm{IM}}}}{1-r_{22}\left(\cos\tilde{\phi}-\mathrm{i}\cdot\sin\tilde{\phi}\right)e^{2L\cdot\tilde{k}_{\mathrm{IM}}}} \right|, \tag{B2}$$

where $\tilde{\phi}=2\tilde{k}_{\mathrm{RE}}L-3\pi/2$. According to Eq. (B2), we can get

$$\begin{aligned}\lambda_s = \Big| & a + amt_{12}t_{21}e^{4L\cdot\tilde{k}_{\mathrm{IM}}} + mt_{12}t_{21}\cos\tilde{\phi}e^{2L\cdot\tilde{k}_{\mathrm{IM}}} \\ & +\mathrm{i}\left(b+bmt_{12}t_{21}e^{4L\cdot\tilde{k}_{\mathrm{IM}}} - mt_{12}t_{21}\sin\tilde{\phi}e^{2L\cdot\tilde{k}_{\mathrm{IM}}}\right)\Big|\end{aligned}, \tag{B3}$$

where $a=\mathrm{Re}\left(r_{11}\right)$, $b=\mathrm{Im}\left(r_{11}\right)$, $m=\left[\left(a^2+b^2\right)e^{4L\cdot\tilde{k}_{\mathrm{IM}}}+2\left(a\cos\tilde{\phi}-b\sin\tilde{\phi}\right)e^{2L\cdot\tilde{k}_{\mathrm{IM}}}+1\right]^{-1}$.

When the eigenvalue $\lambda_s$ equals 0, we get

$$\begin{cases} a + amt_{12}t_{21}e^{4L\cdot\tilde{k}_{\mathrm{IM}}} + mt_{12}t_{21}\cos\tilde{\phi}e^{2L\cdot\tilde{k}_{\mathrm{IM}}} = 0 \\ b+bmt_{12}t_{21}e^{4L\cdot\tilde{k}_{\mathrm{IM}}} - mt_{12}t_{21}\sin\tilde{\phi}e^{2L\cdot\tilde{k}_{\mathrm{IM}}} = 0 \end{cases}. \tag{B4}$$

The equation set (B4) has non-zero solutions, we can get

$$\tan\tilde{\phi}=\frac{-b}{a}. \tag{B5}$$

According to Eq. (B5), we can get

$$\varphi=\frac{3\pi}{4}-\frac{1}{2}\arg\left(r_{11}\right)+n\pi, \quad n\geq 1, \tag{B6}$$

where $\varphi = L\cdot\tilde{k}_{\mathrm{RE}}$. Solving this equation set (B4), we get

$$2L\cdot\tilde{k}_{\mathrm{IM}} = \mathrm{In}\left|r_{11}\right|. \tag{B7}$$

From Eq. (B6) and (B7), we obtain the complex wavenumber $\Omega_{\mathrm{Zero}}^{\mathrm{Lossless}}$, which corresponds to the Zero in the complex wavenumber plane, i.e.,

$$\Omega_{\mathrm{Zero}}^{\mathrm{Lossless}} \equiv \varphi + \frac{\mathrm{In}\left|r_{11}\right|}{2}\cdot\mathrm{i}. \tag{B8}$$

## Appendix C. PAC in the lossy elastic wave system

The wavenumber in the waveguide resonator with the loss fact $\eta$ is

$$k_2=\left(\frac{\rho_s d_s\omega^2}{D_s\left(1+\eta^2\right)}\left(1-\eta\mathrm{i}\right)\right)^{\frac{1}{4}}=\left(\frac{\rho_s d_s\omega^2}{D_s}\right)^{\frac{1}{4}}\left(\frac{1}{\left(1+\eta^2\right)}\right)^{\frac{1}{4}}\left(1-\eta\mathrm{i}\right)^{\frac{1}{4}}. \tag{C1}$$

According to $\Omega=k_2L=\left(\tilde{k}_{\mathrm{RE}}+\tilde{k}_{\mathrm{IM}}\mathrm{i}\right)L$, we can get

$$\Omega=\left[\mathrm{Re}\left(k_2\right)+\mathrm{Im}\left(k_2\right)\mathrm{i}\right]L. \tag{C2}$$

According to Eq. (C2), Eq. (9), and Eq. (12), we get

$$\begin{aligned}&\mathrm{Im}\left(k_2\right)L=-\varsigma=\frac{\mathrm{In}\left|r_{11}\right|}{2}\\&\mathrm{Re}\left(k_2\right)L=\varphi\end{aligned}. \tag{C3}$$

According to Eq. (C1) and Eq. (C3), we can get

$$\frac{\mathrm{Re}\left(\wp\right)}{\mathrm{Im}\left(\wp\right)}\equiv\frac{2\varphi}{\mathrm{In}\left|r_{11}\right|}, \tag{C4}$$

where $\wp=\sqrt[4]{1-\eta\cdot\mathrm{i}}$.

## Appendix D. The thickness ratio $\varepsilon_d$ is a constant regarding $\eta$

The most practical metal alloys or composite structures have small internal losses, as described by the loss factor of less than 0.1. We can get

$$\wp=\sqrt[4]{1-\eta\cdot\mathrm{i}}\approx1-\eta\cdot\mathrm{i}/4. \tag{D1}$$

Substituting Eq. (D1) into Eq. (C4), we obtain

$$\left|r_{11}\right|=e^{-\varphi\eta/2}. \tag{D2}$$

Eq. (A5) is simplified to

$$\left|r_{11}\right|=\frac{1-2\tilde{\varepsilon}^4}{2\tilde{\varepsilon}^4+2\tilde{\varepsilon}^3+1}, \tag*{(D3}$$

where $\tilde{\varepsilon}=\sqrt{\varepsilon_d}=\sqrt{d_2/d_1}$. According to Eqs. (D2) and (, we obtain

$$\left(\vartheta+2\right)\tilde{\varepsilon}^4+\vartheta\tilde{\varepsilon}^3+\left(\vartheta-2\right)/2=0, \tag{D4}$$

where $\vartheta=2e^{\left(-\varphi\eta/2\right)}$.

Solving the quartic equation of one unknown (D4) by the Ferrari method, we get the thickness ratio $\varepsilon_d$

$$\varepsilon_d = \left( \frac{-\vartheta - \sqrt{\vartheta^2 + \psi_1} + \sqrt{2\vartheta^2 + \psi_2}}{4\vartheta + 8} \right)^2, \tag{D5}$$

where

$$\begin{aligned} &\vartheta = 2e^{(-\varphi\eta/2)} \\ &\psi_1 = \frac{\sqrt[3]{z_1} - \sqrt[3]{z_2}}{3} \\ &\psi_2 = -\psi_1 + \frac{2\sqrt{z_3}}{3} \end{aligned} \quad . \tag{D6}$$

$$\begin{aligned} &z_1 = 3z_A\vartheta^2 - 3(z_B - \sqrt{{z_B}^2 - 4z_A z_C})/2 \\ &z_2 = -3z_A\vartheta^2 + 3(z_B + \sqrt{{z_B}^2 - 4z_A z_C})/2 \\ &z_3 = 9\vartheta^4 - 3\vartheta^2(\sqrt[3]{z_1} - \sqrt[3]{z_2}) + (\sqrt[3]{z_1} - \sqrt[3]{z_2})^2 - 3z_A \\ &z_A = -3z_0 + 9\vartheta^4 \\ &z_B = 3\vartheta^2 z_0 - 9\vartheta^6 \\ &z_C = {z_0}^2 - 9\vartheta^8 \\ &z_0 = 3\vartheta^4 - 32\cdot(\vartheta + 2)^3(\vartheta - 2) \end{aligned} \quad . \tag{D7}$$

## Appendix E. The scattering matrix of the elastic plate system

In the *x*-axis direction shown in Fig. 4(a), the slope $\varphi$, bending moment *M*, and shear force *V*, in the two-dimension plate model are rewritten as

$$\varphi_x^{(\mathrm{I})} = \frac{\partial w^{(\mathrm{I})}}{\partial x}, \tag{E1}$$

$$M_x^{(\mathrm{I})} = \begin{cases} D\left( \dfrac{\partial^2 w^{(\mathrm{I})}}{\partial x^2} + \upsilon \dfrac{\partial^2 w^{(\mathrm{I})}}{\partial y^2} \right) & |y - y_m| \le p/2 \\ 0 & |y - y_m + p/2| \le (l - p)/2 \end{cases}, \tag{E2}$$

$$V_x^{(\mathrm{I})} = \begin{cases} -D\left[ \dfrac{\partial^3 w^{(\mathrm{I})}}{\partial x^3} + (2 - \upsilon) \dfrac{\partial^3 w^{(\mathrm{I})}}{\partial x \partial y^2} \right] & y - y_m \le |p/2| \\ 0 & y - y_m + p/2 \le |(l - p)/2| \end{cases}, \tag{E3}$$

where $y_m = (m-1)l$.

By applying the continuous boundary conditions of the *x*-component of displacement at the interface $\tilde{l}_3$ of *x*=0, and integrating it into the *y*-direction in the region $y - y_m \le |p/2|$, we can get

$$\begin{pmatrix} {}_1P^1 \\ \vdots \\ {}_1P^m \\ \vdots \\ {}_1P^M \end{pmatrix} + \begin{pmatrix} {}_1\mathbf{H}_1^1 \cdots & {}_1\mathbf{H}_j^1 & \cdots & {}_1\mathbf{H}_J^1 \\ \vdots & \vdots & & \vdots \\ {}_1\mathbf{H}_1^m \cdots & {}_1\mathbf{H}_j^m & \cdots & {}_1\mathbf{H}_J^m \\ \vdots & \vdots & & \vdots \\ {}_1\mathbf{H}_1^M \cdots & {}_1\mathbf{H}_j^M & \cdots & {}_1\mathbf{H}_J^M \end{pmatrix} \mathbf{T}^{(\mathrm{I})} = \begin{pmatrix} {}_1\mathbf{q}^1 & & & & \\ & \ddots & & & \\ & & {}_1\mathbf{q}^m & & \\ & & & \ddots & \\ & & & & {}_1\mathbf{q}^M \end{pmatrix} \mathbf{T}_{\mathrm{L}}^{(\mathrm{II})}, \qquad \text{(E4)}$$

where ${}_1\mathbf{H}_j^m(m, j) = \left[ e^{-\mathrm{i}k_{yj}\cdot y_m} \operatorname{sinc}\left(k_{yj} \cdot p/2\right),\ e^{-\mathrm{i}k_{yj}\cdot y_m} \operatorname{sinc}\left(k_{yj} \cdot p/2\right) \right]$, ${}_1\mathbf{q}^m = [1,\ 1,\ 1,\ 1]$, ${}_1P^m(m) = e^{-\mathrm{i}k_{y0}\cdot y_m} \operatorname{sinc}\left(k_{y0} \cdot p/2\right)$. Similarly, for the continuous boundary conditions of *x*-components of the slop at the interface $\tilde{l}_3$ of *x*=0, we can get

$$\begin{pmatrix} {}_2P^1 \\ \vdots \\ {}_2P^m \\ \vdots \\ {}_2P^M \end{pmatrix} + \begin{pmatrix} {}_2\mathbf{H}_1^1 \cdots & {}_2\mathbf{H}_j^1 & \cdots & {}_2\mathbf{H}_J^1 \\ \vdots & \vdots & & \vdots \\ {}_2\mathbf{H}_1^m \cdots & {}_2\mathbf{H}_j^m & \cdots & {}_2\mathbf{H}_J^m \\ \vdots & \vdots & & \vdots \\ {}_2\mathbf{H}_1^M \cdots & {}_2\mathbf{H}_j^M & \cdots & {}_2\mathbf{H}_J^M \end{pmatrix} \mathbf{T}^{(\mathrm{I})} = \begin{pmatrix} {}_2\mathbf{q}^1 & & & & \\ & \ddots & & & \\ & & {}_2\mathbf{q}^m & & \\ & & & \ddots & \\ & & & & {}_2\mathbf{q}^M \end{pmatrix} \mathbf{T}_{\mathrm{L}}^{(\mathrm{II})}, \qquad \text{(E5)}$$

where ${}_2P^m(m) = -\mathrm{i}k_{x0} e^{-\mathrm{i}k_{y0}\cdot y_m} \cdot \operatorname{sinc}\left(k_{y0} \cdot p/2\right)$, ${}_2\mathbf{q}^m = [-\mathrm{i}k_1,\ -k_1,\ \mathrm{i}k_1,\ k_1]$, ${}_2\mathbf{H}_j^m(m, j) = \left[ \mathrm{i}k_{xj} e^{-\mathrm{i}k_{yj}\cdot y_m} \cdot \operatorname{sinc}\left(k_{yj} \cdot p/2\right),\ \bar{k}_{xj} e^{-\mathrm{i}k_{yj}\cdot y_m} \cdot \operatorname{sinc}\left(k_{yj} \cdot p/2\right) \right]$.

By applying the continuous boundary conditions of *x*-components of bending moment at the interface $\tilde{l}_3$ of *x*=0, and using the orthogonal relationship of the waveshapes and integrating to the *y*-direction at the region $0 \le y \le g$, we can get

$$\begin{pmatrix} {}_3P^1 \\ \vdots \\ {}_3P^j \\ \vdots \\ {}_3P^J \end{pmatrix} + \begin{pmatrix} {}_3\mathbf{H}_1 & & & & \\ & \ddots & & & \\ & & {}_3\mathbf{H}_j & & \\ & & & \ddots & \\ & & & & {}_3\mathbf{H}_J \end{pmatrix} \mathbf{T}^{(\mathrm{I})} = \begin{pmatrix} {}_3\mathbf{q}_1^1 \cdots & {}_3\mathbf{q}_1^m & \cdots & {}_3\mathbf{q}_1^M \\ \vdots & \vdots & & \vdots \\ {}_3\mathbf{q}_j^1 \cdots & {}_3\mathbf{q}_j^m & \cdots & {}_3\mathbf{q}_j^M \\ \vdots & \vdots & & \vdots \\ {}_3\mathbf{q}_J^1 \cdots & {}_3\mathbf{q}_J^m & \cdots & {}_3\mathbf{q}_J^M \end{pmatrix} \mathbf{T}_{\mathrm{L}}^{(\mathrm{II})}, \qquad \text{(E6)}$$

where ${}_3\mathbf{q}_j^m\left(m,j\right)=\left[-\varsigma_1,\ \varsigma_1,\ -\varsigma_1,\ \varsigma_1\right]$, ${}_3\mathbf{H}_j\left(j\right)=\left[g\cdot\left(-k_{xj}{}^2-\upsilon k_{yj}{}^2\right),\ \tilde{k}_{xj}{}^2-\upsilon k_{yj}{}^2\right]$, $\varsigma_1=pk_1{}^2\sin c\left(k_{yj}\cdot p/2\right)\cdot e^{ik_{yj}y_m}$, ${}_3P^j=g\cdot\left(-k_{x0}{}^2-\upsilon k_{y0}{}^2\right)$. Similarly, for the continuous boundary conditions of *x*-components of shear force at the interface $\tilde{l}_3$ of *x*=0, we can get

$$\begin{pmatrix} {}_4P^1 \\ \vdots \\ {}_4P^j \\ \vdots \\ {}_4P^J \end{pmatrix}+\begin{pmatrix} {}_4\mathbf{H}_1 & & & & \\ & \ddots & & & \\ & & {}_4\mathbf{H}_j & & \\ & & & \ddots & \\ & & & & {}_4\mathbf{H}_J \end{pmatrix}\mathbf{T}^{(\mathrm{I})}=\begin{pmatrix} {}_4\mathbf{q}_1^1\cdots & {}_4\mathbf{q}_1^m & \cdots & {}_4\mathbf{q}_1^M \\ \vdots & \vdots & & \vdots \\ {}_4\mathbf{q}_j^1\cdots & {}_4\mathbf{q}_j^m & \cdots & {}_4\mathbf{q}_j^M \\ \vdots & \vdots & & \vdots \\ {}_4\mathbf{q}_J^1\cdots & {}_4\mathbf{q}_J^m & \cdots & {}_4\mathbf{q}_J^M \end{pmatrix}\mathbf{T}_{\mathrm{L}}^{(\mathrm{II})},\qquad \text{(E7)}$$

where ${}_4\mathbf{q}_j^m\left(m,j\right)=\left[\mathrm{i}\cdot\varsigma_2,\ -\varsigma_2,\ -\mathrm{i}\cdot\varsigma_2,\ \varsigma_2\right]$, ${}_4P^j=g\cdot\left[-\mathrm{i}k_{x0}{}^3-\left(2-\upsilon\right)\mathrm{i}k_{x0}k_{y0}{}^2\right]$, ${}_4\mathbf{H}_j\left(j\right)=g\cdot\left\{\left[-\mathrm{i}k_{xj}{}^3-\left(2-\upsilon\right)\mathrm{i}k_{xj}k_{yj}{}^2\right],\ \left[\tilde{k}_{xj}{}^3-\left(2-\upsilon\right)\tilde{k}_{xj}k_{yj}{}^2\right]\right\}$
$\varsigma_2=pk_1^3\sin c(k_{yj}\cdot p/2)e^{\mathrm{i}k_{yj}y_m}$.

In the region (II) of one supercell, the transfer equation for waves propagating from the left to the right interface of the $m^{\text{th}}$ waveguide can be expressed as

$$\mathbf{T}_{\mathrm{R}}^{(\mathrm{II})}=\begin{pmatrix} \mathbf{I}^1 & & & & \\ & \ddots & & & \\ & & \mathbf{I}^m & & \\ & & & \ddots & \\ & & & & \mathbf{I}^M \end{pmatrix}\mathbf{T}_{\mathrm{L}}^{(\mathrm{II})}=\mathbf{N}\cdot\mathbf{T}_{\mathrm{L}}^{(\mathrm{II})},\qquad \text{(E8)}$$

where $\mathbf{I}^m=\begin{pmatrix} \mathrm{i}e^{-\mathrm{i}k_1h_m} & & & \\ & -e^{-k_1h_m} & & \\ & & -\mathrm{i}e^{\mathrm{i}k_1h_m} & \\ & & & e^{k_1h_m} \end{pmatrix}$.

By applying the continuous boundary conditions of the *x*-component of displacement at the interface $\tilde{l}_4$, and integrating to the *z*-direction in the region $z\le\left|d_1/2\right|$, we can get

$$\begin{pmatrix} {}_5\mathbf{q}^N & & & & \\ & \ddots & & & \\ & & {}_5\mathbf{q}^N & & \\ & & & \ddots & \\ & & & & {}_5\mathbf{q}^N \end{pmatrix}_{M\times M} \cdot \mathbf{T}_{\mathrm{R}}^{(\mathrm{II})} = \begin{pmatrix} {}_5\mathbf{p}^N & & & & \\ & \ddots & & & \\ & & {}_5\mathbf{p}^N & & \\ & & & \ddots & \\ & & & & {}_5\mathbf{p}^N \end{pmatrix}_{M\times M} \cdot \mathbf{T}^{(\mathrm{III})}, \quad \text{(E9)}$$

where $${}_5\mathbf{q}^N = \begin{bmatrix} 1 & 1 & 1 & 1 \\ 1 & 1 & 1 & 1 \\ \vdots & \vdots & \vdots & \vdots \\ 1 & 1 & 1 & 1 \end{bmatrix}_{N\times 4}, \qquad {}_5\mathbf{p}^N = \begin{pmatrix} {}_5\mathbf{p}^1 & & & & \\ & \ddots & & & \\ & & {}_5\mathbf{p}^n & & \\ & & & \ddots & \\ & & & & {}_5\mathbf{p}^N \end{pmatrix},$$

$${}_5\mathbf{p}^n(n) = \left[1 - \mathrm{i}e^{-2\mathrm{i}k_2\cdot L_n} + (1-\mathrm{i})e^{-(\mathrm{i}+1)\cdot k_2 L_n}, 1 + \mathrm{i}e^{-2k_2\cdot L_n} + (1+\mathrm{i})e^{-(\mathrm{i}+1)k_2\cdot L_n}\right].$$

By applying the continuous boundary conditions of the *x*-component of slop at the interface $\tilde{l}_4$, and integrating it to the *z*-direction in the region $z \le |d_1/2|$, we can get

$$\begin{pmatrix} {}_6\mathbf{q}^N & & & & \\ & \ddots & & & \\ & & {}_6\mathbf{q}^N & & \\ & & & \ddots & \\ & & & & {}_6\mathbf{q}^N \end{pmatrix}_{M\times M} \cdot \mathbf{T}_{\mathrm{R}}^{(\mathrm{II})} = \begin{pmatrix} {}_6\mathbf{p}^N & & & & \\ & \ddots & & & \\ & & {}_6\mathbf{p}^N & & \\ & & & \ddots & \\ & & & & {}_6\mathbf{p}^N \end{pmatrix}_{M\times M} \cdot \mathbf{T}^{(\mathrm{III})}, \quad \text{(E10)}$$

where $${}_6\mathbf{q}^N = \begin{bmatrix} -\mathrm{i}k_1 & -k_1 & \mathrm{i}k_1 & k_1 \\ -\mathrm{i}k_1 & -k_1 & \mathrm{i}k_1 & k_1 \\ \vdots & \vdots & \vdots & \vdots \\ -\mathrm{i}k_1 & -k_1 & \mathrm{i}k_1 & k_1 \end{bmatrix}_{N\times 4}, \qquad {}_6\mathbf{p}^N = \begin{pmatrix} {}_6\mathbf{p}^1 & & & & \\ & \ddots & & & \\ & & {}_6\mathbf{p}^n & & \\ & & & \ddots & \\ & & & & {}_6\mathbf{p}^N \end{pmatrix},$$

$${}_6\mathbf{p}^n(n) = \left[-\mathrm{i}k_2 + k_2 e^{-2\mathrm{i}k_2\cdot L_n} + (1-\mathrm{i})k_2 e^{-(\mathrm{i}+1)\cdot k_2 L_n}, -k_2 + \mathrm{i}k_2 e^{-2k_2\cdot L_n} + (\mathrm{i}-1)k_2 e^{-(\mathrm{i}+1)k_2\cdot L_n}\right].$$

By applying the continuous boundary conditions of the *x*-component of bending moment at the interface $\tilde{l}_4$, and integrating to the *z*-direction in the region $z \le |d_1/2|$, we can get

$$\begin{pmatrix} {}_7\mathbf{q} & & & & \\ & \ddots & & & \\ & & {}_7\mathbf{q} & & \\ & & & \ddots & \\ & & & & {}_7\mathbf{q} \end{pmatrix}_{M\times M} \cdot \mathbf{T}_{\mathrm{R}}^{(\mathrm{II})} = \begin{pmatrix} {}_7\mathbf{p}^N & & & & \\ & \ddots & & & \\ & & {}_7\mathbf{p}^N & & \\ & & & \ddots & \\ & & & & {}_7\mathbf{p}^N \end{pmatrix}_{M\times M} \cdot \mathbf{T}^{(\mathrm{III})}, \quad \text{(E11)}$$

where ${}_7\mathbf{q}=D_1\left[-k_1,\ k_1,\ -k_1,\ k_1\right]$ , ${}_7\mathbf{p}^N=\left[{}_7\mathbf{q}^1,\cdots,{}_7\mathbf{q}^n,\ \cdots,{}_7\mathbf{q}^N\right]$ ,

$${}_7\mathbf{q}^n(n)=D_2\left[-k_2{}^2+\mathrm{i}k_2{}^2e^{-2\mathrm{i}k_2\cdot L_n}+(1-\mathrm{i})k_2{}^2e^{-(\mathrm{i}+1)\cdot k_2L_n},k_2{}^2+\mathrm{i}k_2{}^2e^{-2k_2\cdot L_n}-(1+\mathrm{i})k_2{}^2e^{-(\mathrm{i}+1)k_2\cdot L_n}\right]$$

By applying the continuous boundary conditions of the *x*-component of shear force at the interface $\tilde{l}_4$, and integrating to the *z*-direction in the region $z\le\left|d_1/2\right|$, we can get

$$\begin{pmatrix} {}_8\mathbf{q} & & & & \\ & \ddots & & & \\ & & {}_8\mathbf{q} & & \\ & & & \ddots & \\ & & & & {}_8\mathbf{q} \end{pmatrix}_{M\times M} \cdot \mathbf{T}_{\mathrm{R}}^{(\mathrm{II})} = \begin{pmatrix} {}_8\mathbf{p}^N & & & & \\ & \ddots & & & \\ & & {}_8\mathbf{p}^N & & \\ & & & \ddots & \\ & & & & {}_8\mathbf{p}^N \end{pmatrix}_{M\times M} \cdot \mathbf{T}^{(\mathrm{III})}, \quad \text{(E12)}$$

where ${}_8\mathbf{q}=D_1\left[\mathrm{i}k_1,\ -k_1,\ -\mathrm{i}k_1,\ k_1\right]$ , ${}_8\mathbf{p}^N=\left[{}_8\mathbf{q},\cdots,{}_8\mathbf{q},\ \cdots,{}_8\mathbf{q}\right]_{N\times 1}$ ,

$${}_8\mathbf{q}(n)=D_2\left[\mathrm{i}k_2{}^3-k_2{}^3e^{-2\mathrm{i}k_2\cdot L_n}+(1-\mathrm{i})k_2{}^3e^{-(\mathrm{i}+1)\cdot k_2L_n},-k_2{}^3+\mathrm{i}k_2{}^3e^{-2k_2\cdot L_n}+(1-\mathrm{i})k_2{}^3e^{-(\mathrm{i}+1)k_2\cdot L_n}\right].$$

Eqs. (E4)-(E7) and Eqs. (E9)-(E12), in turn, can be rewritten as

$$\begin{aligned} \mathbf{P_1}+\mathbf{H}_1\mathbf{T}^{(\mathrm{I})} &= \mathbf{Q}_1\mathbf{T}_{\mathrm{L}}^{(\mathrm{II})} \\ \mathbf{P_2}+\mathbf{H}_2\mathbf{T}^{(\mathrm{I})} &= \mathbf{Q}_2\mathbf{T}_{\mathrm{L}}^{(\mathrm{II})} \\ \mathbf{P_3}+\mathbf{H}_3\mathbf{T}^{(\mathrm{I})} &= \mathbf{Q}_3\mathbf{T}_{\mathrm{L}}^{(\mathrm{II})} \\ \mathbf{P_4}+\mathbf{H}_4\mathbf{T}^{(\mathrm{I})} &= \mathbf{Q}_4\mathbf{T}_{\mathrm{L}}^{(\mathrm{II})} \\ \mathbf{Q}_5\mathbf{N}\mathbf{T}_{\mathrm{L}}^{(\mathrm{II})} &= \mathbf{P}_5\mathbf{T}^{(\mathrm{III})} \\ \mathbf{Q}_6\mathbf{N}\mathbf{T}_{\mathrm{L}}^{(\mathrm{II})} &= \mathbf{P}_6\mathbf{T}^{(\mathrm{III})} \\ \mathbf{Q}_7\mathbf{N}\mathbf{T}_{\mathrm{L}}^{(\mathrm{II})} &= \mathbf{P}_7\mathbf{T}^{(\mathrm{III})} \\ \mathbf{Q}_8\mathbf{N}\mathbf{T}_{\mathrm{L}}^{(\mathrm{II})} &= \mathbf{P}_8\mathbf{T}^{(\mathrm{III})} \end{aligned} . \quad \text{(E13)}$$

According to Eq. (E13), we can get a linear equation set about $\mathbf{T}^{(\mathrm{I})}$, $\mathbf{T}_{\mathrm{L}}^{(\mathrm{II})}$ and $\mathbf{T}^{(\mathrm{III})}$

$$\mathbf{G}_1 \cdot \begin{pmatrix} \mathbf{T}^{(\mathrm{I})} \\ \mathbf{T}_{\mathrm{L}}^{(\mathrm{II})} \\ \mathbf{T}^{(\mathrm{III})} \end{pmatrix} = \mathbf{G}_2, \tag{E14}$$

where

$$\mathbf{G}_1 = \begin{pmatrix} -\mathbf{H}_1^{\mathrm{T}} & -\mathbf{H}_2^{\mathrm{T}} & -\mathbf{H}_3^{\mathrm{T}} & -\mathbf{H}_4^{\mathrm{T}} & O & O & O & O \\ \mathbf{Q}_1^{\mathrm{T}} & \mathbf{Q}_2^{\mathrm{T}} & \mathbf{Q}_3^{\mathrm{T}} & \mathbf{Q}_4^{\mathrm{T}} & (\mathbf{Q}_5\mathbf{N})^{\mathrm{T}} & (\mathbf{Q}_6\mathbf{N})^{\mathrm{T}} & (\mathbf{Q}_7\mathbf{N})^{\mathrm{T}} & (\mathbf{Q}_8\mathbf{N})^{\mathrm{T}} \\ O & O & O & O & -\mathbf{P}_5^{\mathrm{T}} & -\mathbf{P}_6^{\mathrm{T}} & -\mathbf{P}_7^{\mathrm{T}} & -\mathbf{P}_8^{\mathrm{T}} \end{pmatrix}^{\mathrm{T}},$$

$$\mathbf{G}_2 = \begin{pmatrix} \mathbf{P}_1 & \mathbf{P}_2 & \mathbf{P}_3 & \mathbf{P}_4 & O \end{pmatrix}^{\mathrm{T}}.$$

where $\mathbf{G}_1$ are square matrices of size $(2J+4M+2MN)\times(2J+4M+2MN)$, and $\mathbf{G}_2$ is a column vector of size $(2J+4M+2MN)$. The corresponding amplitudes of diffraction modes can be calculated by solving Eq. (E14).

## Appendix F. The scattering matrix of the elastic beam system

When the unit number in the metasurface and the diffraction mode number are set to $M$=1 and $J$=1, respectively, the propagation constant $\beta$ changes from $\beta^4 = \rho d / \left[ D\left(1-\upsilon^2\right)\right]$ to $\beta^4 = \rho d / D$, Eq. (E14) can be reduced to the scattering equation of the background beam

$$^{b}\mathbf{G}_1 \cdot \begin{pmatrix} ^{b}\mathbf{T}^{(\mathrm{I})} \\ ^{b}\mathbf{T}_{\mathrm{L}}^{(\mathrm{II})} \\ ^{b}\mathbf{T}^{(\mathrm{III})} \end{pmatrix} = {}^{b}\mathbf{G}_2, \tag{F1}$$

where $^{b}\mathbf{G}_1$ are square matrices of size $(2+4+2N)\times(2+4+2N)$, and $^{b}\mathbf{G}_2$ is a column vector of size $(2+4+2N)$. The reflection coefficient equals $\Re_0$. The absorption coefficient of the LEM is $\alpha_b = 1 - \left|\Re_0\right|^2$.

## Appendix G. Phase shift of $3\pi/2$ at the free hard boundary

We set an incident flexural wave of $1 \cdot e^{-\mathrm{i}(kx-\omega t)}$ at the left side of the hard boundary $\tilde{l}_2$, so the scattering wave field with evanescent wave hybridization can be expressed as follows:

$$w_\mathrm{b}(x) = \left(1e^{-\mathrm{i}kx} + r_\mathrm{b} + \tilde{r}_\mathrm{b}\right)e^{\mathrm{i}\omega t} = \left(1e^{-\mathrm{i}kx} + R_\mathrm{b}e^{\mathrm{i}kx} + \tilde{R}_\mathrm{b}e^{kx}\right)e^{\mathrm{i}\omega t}, \tag{G1}$$

where the subscript ~ represents an evanescent wave. Setting up a local coordinate system $x$=0 at the boundary $\tilde{l}_2$, according to bending moment $M = Dw''_\mathrm{b}$ and shear forces $V = -Dw'''_\mathrm{b}$ are zero at the free boundary $\tilde{l}_2$, we obtain

$$\begin{cases} -1 - R_\mathrm{b} + \tilde{R}_\mathrm{b} = 0 \\ \mathrm{i} - \mathrm{i}R_\mathrm{b} + \tilde{R}_\mathrm{b} = 0 \end{cases}, \tag{G2}$$

From Eq. (G2), we get $R_b = -\mathrm{i} = 1 \cdot e^{\mathrm{i}(3\pi/2)}$, i.e., the propagation reflection wave has the phase of $3\pi/2$. The incident flexural wave of $1 \cdot e^{\mathrm{i}\omega t}$ has the phase of 0. Therefore, the propagation reflection wave has a phase shift of $3\pi/2$ at the free hard boundary, due to the evanescent wave hybridization.

## Appendix H. Experimental measurements

As shown in Fig. 4h, the PZT patches are driven by a signal generator (Tektronix AFG3022C). The blue-tack layer is bonded to the bottom of the plate specimen to absorb the downward propagating flexural wave excited by the PZT patch and the reflected flexural wave from the designed structure at the top. The length of blue-tack in the direction of propagation waves is 50 mm, which can be equivalent to a non-reflection boundary of flexural waves within the frequency range of the experiment. The specimen surface is held perpendicular to the laser beam from PSV-500 scanning laser Doppler vibrometer through a C-clamp supporting the plate applied to the lower edge, as shown in Fig. 4h. The PSV-500 scanning head records the out-of-plane complex velocities of two measurement points in the far-field of the incident direction using the measurement mode "FFT". An ensemble average with 20 samples is used at every measurement point to ensure signal quality. The measured complex velocities in the two points are $v^1$ and $v^2$, respectively. We can calculate the reflection coefficient as $\tilde{r} = \left(H_{12} - e^{-\mathrm{i}\hat{k}_b\bar{s}_1}\right)\cdot e^{\mathrm{i}2(\bar{s}_1+\bar{s}_2)\cdot\hat{k}_b} \Big/ \left(e^{-\mathrm{i}\hat{k}_b\bar{s}_1} - H_{12}\right)$, where $\bar{s}_1$ and $\bar{s}_2$ are the distance between the two points, $H_{12} = v^2/v^1$. $\hat{k}_b$ is the measured wavenumber of the flexural wave in the host structure. The absorption coefficient of flexural waves can be calculated by $\tilde{\alpha} = 1 - |\tilde{r}|^2$.

## Appendix I. The geometry of specimens in the experiments

For six single resonator specimens with different lengths, we name them as "1st single resonator specimen", "2nd single resonator specimen", "3rd single resonator specimen", "4th single resonator specimen", "5th single resonator specimen", and "6th single resonator specimen". Their resonator thicknesses are $d_2$, and their resonator lengths are $L_1$, $L_2$, $L_3$, $L_4$, $L_5$, and $L_6$, respectively. Specific geometric parameters of the resonators are shown in Table S1.

Table S1 The geometric parameters of specimens in the experiments. All parameters are in units of mm.

| $d_1$ | $d_2$ | $L_1$ | $L_2$ | $L_3$ | $L_4$ | $L_5$ | $L_6$ | $b$ | $g$ | $S_1$ | $S_2$ | $S_3$ |
|---|---|---|---|---|---|---|---|---|---|---|---|---|
| 3.0 | 0.2 | 6.6 | 6.8 | 7.0 | 7.1 | 7.2 | 7.3 | 2.5 | 9 | 1.5 | 7.5 | 13.5 |

## Appendix J. Absorption spectrums of LEMs in elastic beams with different materials

Our proposed design method is universal and applicable to almost all solid beams or plates composed of any material. Based on Eq. (6), we design LEMs in four elastic beams with different materials of concrete, cross-grain wood, plexiglass (PMMA), and Aluminum alloy. These LEMs are defined as the cases from $C_1$ to $C_4$. We show the absorption spectrums in Figure S1. The related material and geometric parameters of the cases from $C_1$ to $C_4$ are shown in Table S2.

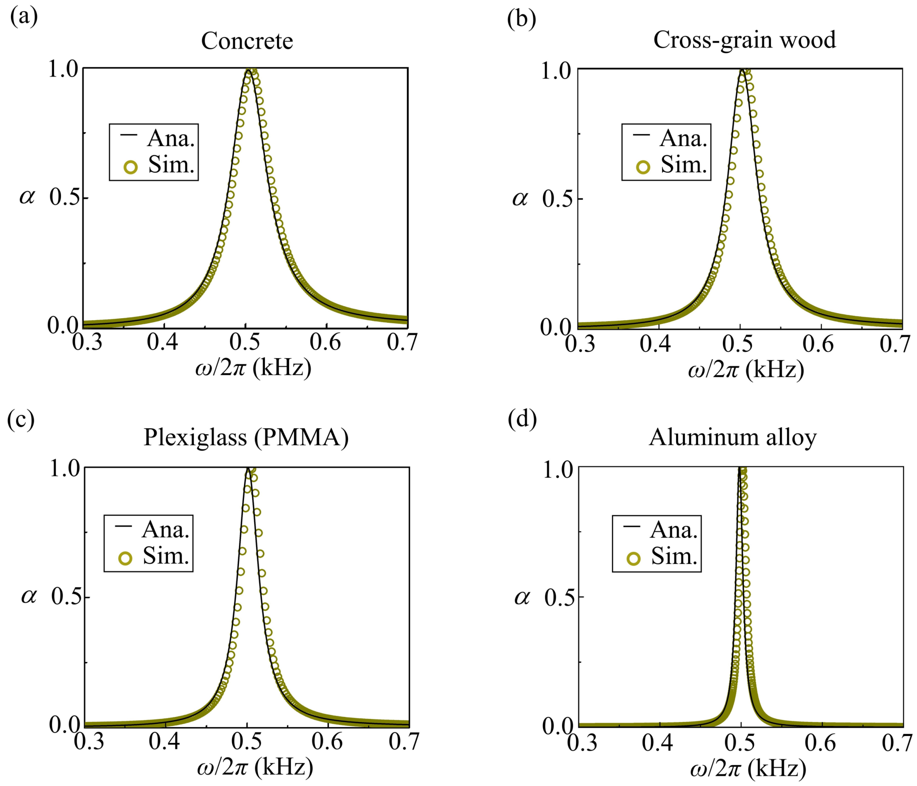

Figure S1. The absorption spectrums of LEMs in four elastic beams made of various materials. The cases from $C_1$ to $C_4$ correspond to (a), (b), (c), and (d), respectively.

Table S2 The material and geometric parameters of the cases from $C_1$ to $C_4$. All geometric parameters are in units of mm.

| | Material | $E$(GPa) | $\rho$(Kg/m$^3$) | $\upsilon$ | $\eta$ | $d_1$ | $d_2$ | $L$ |
|---|---|---|---|---|---|---|---|---|
| $C_1$ | Concrete | 40 | 2500 | 0.30 | 0.05 | 3 | 0.32 | 54.7 |
| $C_2$ | Cross-grain wood | 0.6 | 540 | 0.49 | 0.04 | 3 | 0.30 | 27.2 |

| | | | | | | | | |
|---|---|---|---|---|---|---|---|---|
| $C_3$ | PMMA | 3.16 | 1190 | 0.32 | 0.03 | 3 | 0.25 | 29.6 |
| $C_4$ | Aluminum alloy | 70 | 2700 | 0.33 | 0.01 | 3 | 0.13 | 37.8 |

## Appendix K. Material parameters and numerical simulations

The theoretical models in Figs. 1 - 4 are made of Mn-Cu alloy (Yin et al., 2003), with Young's modulus $E_0 = 72\ \text{GPa}$, Poisson's ratio $\upsilon_0 = 0.34$, density $\rho_0 = 7825\ \text{kg/m}^3$, and the loss factor $\eta_0 = 0.022$. The specimens in the experiments are made of 3D print material of PLA, with Young's modulus $E_{\text{PLA}} = 3.44\ \text{GPa}$, Poisson's ratio $\upsilon_{\text{PLA}} = 0.35$, density $\rho_{\text{PLA}} = 1086.3\ \text{kg/m}^3$, and the loss factor $\eta_{\text{PLA}} = 0.02$ (Cao et al., 2021c).

All simulations are performed by using the COMSOL Multiphysics 5.6 software (Solid Mechanics Module). All outer boundaries have any reflection by PMLs. We obtain the simulated absorption spectrum by post-processing in the same calculation method as the experiment.

## References

Assouar, B., Liang, B., Wu, Y., Li, Y., Cheng, J., Jing, Y., 2018. Acoustic metasurfaces. Nat Rev Mater 3, 460-472.

Cai, M., Painter, O., Vahala, K.J., 2000. Observation of Critical Coupling in a Fiber Taper to a Silica-Microsphere Whispering-Gallery Mode System. Phys Rev Lett 85, 74-77.

Cao, L., Yang, Z., Xu, Y., Chen, Z., Zhu, Y., Fan, S.-W., Donda, K., Vincent, B., Assouar, B., 2021a. Pillared elastic metasurface with constructive interference for flexural wave manipulation. Mech Syst Signal Pr 146, 107035.

Cao, L., Yang, Z., Xu, Y., Fan, S.-W., Zhu, Y., Chen, Z., Li, Y., Assouar, B., 2020. Flexural wave absorption by lossy gradient elastic metasurface. J Mech Phys Solids 143, 104052.

Cao, L., Zhu, Y., Wan, S., Zeng, Y., Li, Y., Assouar, B., 2021b. Perfect absorption of flexural waves induced by bound state in the continuum. Extreme Mechanics Letters 47.

Cao, L., Zhu, Y., Xu, Y., Fan, S.-W., Yang, Z., Assouar, B., 2021c. Elastic bound state in the continuum with perfect mode conversion. J Mech Phys Solids 154, 104502.

Cao, X., Jia, C., Miao, H., Kang, G., Zhang, C., 2021d. Excitation and manipulation of guided shear-horizontal plane wave using elastic metasurfaces. Smart Mater Struct 30, 055013.

Chen, T., Pauly, M., Reis, P.M., 2021. A reprogrammable mechanical metamaterial with stable memory. Nature 589, 386-390.

Chen, W., Kaya Özdemir, Ş., Zhao, G., Wiersig, J., Yang, L., 2017. Exceptional points enhance sensing in an optical microcavity. Nature 548, 192-196.

Cui, Y., Fung, K.H., Xu, J., Ma, H., Jin, Y., He, S., Fang, N.X., 2012. Ultrabroadband light absorption by a sawtooth anisotropic metamaterial slab. Nano Lett 12, 1443-1447.

Deng, J., Zheng, L., 2022. Noise reduction via three types of acoustic black holes. Mech Syst Signal Pr 165, 108323.

Díaz-Rubio, A., Li, J., Shen, C., Cummer, S.A., Tretyakov, S.A., 2019. Power flow-conformal metamirrors for engineering wave reflections. Sci Adv 5, eaau7288.

Dong, H.-W., Shen, C., Zhao, S.-D., Qiu, W., Zheng, H., Zhang, C., Cummer, S.A., Wang, Y.-S., Fang, D., Cheng, L., 2022. Achromatic metasurfaces by dispersion customization for ultra-broadband acoustic beam engineering. National Science Review.

Dong, H.-W., Zhao, S.-D., Miao, X.-B., Shen, C., Zhang, X., Zhao, Z., Zhang, C., Wang, Y.-S., Cheng, L., 2021. Customized broadband pentamode metamaterials by topology optimization. J Mech Phys Solids 152, 104407.

Gao, N., Guo, X., Deng, J., Cheng, B., Hou, H., 2021. Elastic wave modulation of double-leaf ABH beam embedded mass oscillator. Appl Acoust 173, 107694.

Graff, K.F., 1975. Wave motion in elastic solids.

Gu, Z., Gao, H., Cao, P.-C., Liu, T., Zhu, X.-F., Zhu, J., 2021. Controlling Sound in Non-Hermitian Acoustic Systems. Phys Rev Appl 16, 057001.

Hu, B., Zhang, Z., Zhang, H., Zheng, L., Xiong, W., Yue, Z., Wang, X., Xu, J., Cheng, Y., Liu, X., 2021a. Non-Hermitian topological whispering gallery. Nature 597, 655-659.

Hu, B., Zhang, Z., Zhang, H., Zheng, L., Xiong, W., Yue, Z., Wang, X., Xu, J., Cheng, Y., Liu, X., Christensen, J., 2021b. Non-Hermitian topological whispering gallery. Nature 597, 655-659.

Huang, S., Zhou, Z., Li, D., Liu, T., Wang, X., Zhu, J., Li, Y., 2019. Compact broadband acoustic sink with coherently coupled weak resonances. Sci Bull.

Hunt, J.B., Nissen, J.C., 1982. The broadband dynamic vibration absorber. J Sound Vib 83, 573-578.

Jin, Y., Wang, W., Khelif, A., Djafari-Rouhani, B., 2021. Elastic Metasurfaces for Deep and Robust Subwavelength Focusing and Imaging. Phys Rev Appl 15.

Kawabata, K., Shiozaki, K., Ueda, M., Sato, M., 2019. Symmetry and topology in non-Hermitian physics. Phys Rev X 9, 041015.

Kerwin, E.M., 1959. Damping of flexural waves by a constrained viscoelastic layer. The Journal of the Acoustical Society of America 31, 952-962.

Lee, H., Lee, J.K., Seung, H.M., Kim, Y.Y., 2018. Mass-stiffness substructuring of an elastic metasurface for full transmission beam steering. J Mech Phys Solids 112, 577-593.

Leng, J., Gautier, F., Pelat, A., Picó, R., Groby, J.P., Romero-García, V., 2019. Limits of flexural wave absorption by open lossy resonators: reflection and transmission problems. New J Phys 21, 053003.

Li, B., Hu, Y., Chen, J., Su, G., Liu, Y., Zhao, M., Li, Z., 2020a. Efficient Asymmetric Transmission of Elastic Waves in Thin Plates with Lossless Metasurfaces. Phys Rev Appl 14, 054029.

Li, H., Mekawy, A., Krasnok, A., Alù, A., 2020b. Virtual Parity-Time Symmetry. Phys Rev Lett 124, 193901.

Li, J., Wen, X., Sheng, P., 2021a. Acoustic metamaterials. J Appl Phys 129.

Li, X., Chen, Y., Zhu, R., Huang, G., 2021b. An active meta-layer for optimal flexural wave absorption and cloaking. Mech Syst Signal Pr 149.

Li, Y., Shen, C., Xie, Y., Li, J., Wang, W., Cummer, S.A., Jing, Y., 2017. Tunable asymmetric transmission via Lossy acoustic metasurfaces. Phys Rev Lett 119.

Lin, Z., Ramezani, H., Eichelkraut, T., Kottos, T., Cao, H., Christodoulides, D.N., 2011. Unidirectional Invisibility Induced by $\mathcal{P}\mathcal{T}$-Symmetric Periodic Structures. Phys Rev Lett 106, 213901.

Liu, F., Shi, P., Xu, Y., Cao, L., Shen, Y., Yang, Z., 2021. Total reflection of flexural waves by circular meta-slab and its application in vibration isolation. Int J Mech Sci 212, 106806.

Liu, Y., Liang, Z., Zhu, J., Xia, L., Mondain-Monval, O., Brunet, T., Alù, A., Li, J., 2019. Willis Metamaterial on a Structured Beam. Phys Rev X 9, 011040.

Liu, Y.Q., Liang, Z.X., Liu, F., Diba, O., Lamb, A., Li, J.S., 2017. Source illusion devices for flexural lamb waves using elastic metasurfaces. Phys Rev Lett 119.

Ma, G., Yang, M., Xiao, S., Yang, Z., Sheng, P., 2014. Acoustic metasurface with hybrid resonances. Nat Mater 13, 873-878.

McCormick, C.A., Shepherd, M.R., 2019. Design optimization and performance comparison of three styles of one-dimensional acoustic black hole vibration absorbers. J Sound Vib.

Mei, J., Ma, G., Yang, M., Yang, Z., Wen, W., Sheng, P., 2012. Dark acoustic metamaterials as super absorbers for low-frequency sound. Nat Commun 3, 756.

Merkel, A., Theocharis, G., Richoux, O., Romero-García, V., Pagneux, V., 2015. Control of acoustic absorption in one-dimensional scattering by resonant scatterers. Appl Phys Lett 107, 244102.

Muhammad, Lim, C.W., Li, J.T.H., Zhao, Z., 2020. Lightweight architected lattice phononic crystals with broadband and multiband vibration mitigation characteristics. Extreme Mechanics Letters 41, 100994.

Nair, J.M.P., Mukhopadhyay, D., Agarwal, G.S., 2021. Enhanced Sensing of Weak Anharmonicities through Coherences in Dissipatively Coupled Anti-PT Symmetric Systems. Phys Rev Lett 126, 180401.

Pelat, A., Gautier, F., Conlon, S.C., Semperlotti, F., 2020. The acoustic black hole: A review of theory and applications. J Sound Vib.

Romero-García, V., Theocharis, G., Richoux, O., Pagneux, V., 2016. Use of complex frequency plane to design broadband and sub-wavelength absorbers. The Journal of the Acoustical Society of America 139, 3395-3403.

Rong, J., Ye, W., Zhang, S., Liu, Y., 2020. Frequency-Coded Passive Multifunctional Elastic Metasurfaces. Adv Funct Mater, 2005285.

Ruan, Y., Liang, X., 2021. Reflective elastic metasurface for flexural wave based on surface impedance model. Int J Mech Sci.

Sauvan, C., Hugonin, J.P., Maksymov, I.S., Lalanne, P., 2013. Theory of the Spontaneous Optical Emission of Nanosize Photonic and Plasmon Resonators. Phys Rev Lett 110, 237401.

Shen, Y., Xing, Z., Yang, S., Sun, J., 2019. Parameters optimization for a novel dynamic vibration absorber. Mech Syst Signal Pr 133, 106282.

Shen, Y., Xu, Y., Liu, F., Wang, F., Yang, Z., 2021. 3D-printed meta-slab for focusing flexural waves in broadband. Extreme Mechanics Letters 48, 101410.

Sun, J.Q., Jolly, M.R., Norris, M.A., 1995. Passive, adaptive and active tuned vibration absorbers—a survey. J Mech Design 117, 234-242.

Tang, L., Cheng, L., Ji, H., Qiu, J., 2016. Characterization of acoustic black hole effect using a one-dimensional fully-coupled and wavelet-decomposed semi-analytical model. J Sound Vib 374, 172-184.

Wang, C., Sweeney, W.R., Stone, A.D., Yang, L., 2021a. Coherent perfect absorption at an exceptional point. Science 373, 1261-1265.

Wang, K., Dutt, A., Wojcik, C.C., Fan, S., 2021b. Topological complex-energy braiding of non-Hermitian bands. Nature 598, 59-64.

Wang, X., Fang, X., Mao, D., Jing, Y., Li, Y., 2019. Extremely Asymmetrical Acoustic Metasurface Mirror at the Exceptional Point. Phys Rev Lett 123, 214302.

Yang, M., Chen, S., Fu, C., Sheng, P., 2017. Optimal sound-absorbing structures. Mater Horiz 4, 673-680.

Yin, F., Nagai, K., Watanabe, K., Kawahara, K., 2003. The Damping Behavior of Ni Added Mn–Cu Damping Alloys. Mater Trans 44, 1671.

Yuan, S.M., Chen, A.L., Wang, Y.S., 2020. Switchable multifunctional fish-bone elastic metasurface for transmitted plate wave modulation. J Sound Vib 470, 115168.

Zeng, Y., Zhang, S.-Y., Zhou, H.-T., Wang, Y.-F., Cao, L., Zhu, Y., Du, Q.-J., Assouar, B., Wang, Y.-S., 2021. Broadband inverted T-shaped seismic metamaterial. Mater Design 208, 109906.

Zhang, J., Zhang, X., Xu, F., Ding, X., Deng, M., Hu, N., Zhang, C., 2020. Vibration control of flexural waves in thin plates by 3D-printed metasurfaces. J Sound Vib.

Zhao, J., Cui, X., Bonello, B., Djafari-Rouhani, B., Yuan, W., Pan, Y., Ren, J., Zhang, X., Zhong, Z., 2021. Broadband sub-diffraction and ultra-high energy density focusing of elastic waves in planar gradient-index lenses. J Mech Phys Solids 150, 104357.

Zhou, Z., Huang, S., Li, D., Zhu, J., Li, Y., 2021. Broadband impedance modulation via non-local acoustic metamaterials. National Science Review.

Zhu, R., Liu, X.N., Hu, G.K., Sun, C.T., Huang, G.L., 2014. Negative refraction of elastic waves at the deep-subwavelength scale in a single-phase metamaterial. Nat Commun 5, 5510.